
Development of an experimental apparatus for the production and study of ultracold atomic gases of fermionic lithium

Towards quantum simulation of two-dimensional fermionic systems

Candidato: Giacomo Valtolina

Matricola: 709368

Primo Relatore: Prof. G. Benedek



Secondo Relatore: Prof. M. Inguscio

Primo Correlatore: Dr. G. Roati

Secondo Correlatore: Dr. F. Montalenti

Università degli Studi di Milano - Bicocca

Dipartimento di Fisica G. Occhialini

Anno Accademico 2011/2012

Contents

1	Introduction	1
2	Laser Cooling	5
2.1	Overview	5
2.2	The radiative force	7
2.2.1	Radiative pressure and dipole force	10
2.2.2	Force on a moving atom	11
2.3	Optical Molasses	12
2.3.1	Cooling Limit	14
2.4	The Magneto-Optical Trap	15
2.4.1	MOT Doppler Theory	15
2.4.2	The capture range and velocity	17
2.5	Sub Doppler cooling	18
3	Experimental apparatus	23
3.1	Lithium 6	23
3.1.1	Why lithium?	25
3.2	Optical system	29
3.2.1	Laser Sources	29
3.2.2	Saturated Absorption Spectroscopy Cell	31
3.3	Laser Locking	32
3.3.1	Saturated Absorption Spectroscopy	32
3.4	Vacuum system	39
3.4.1	The Oven	40
3.4.2	Differential Pumping	42
3.4.3	The Zeeman slower	43

3.4.4	Science Chamber	48
3.4.5	Bake out procedure	55
4	Experimental Results	57
4.1	Detection with a photodiode	58
4.1.1	Calibration of the photodiode	59
4.2	MOT loading	60
4.3	Detection with a CCD camera	65
4.4	Compressed MOT stage	77
4.5	Phase-space density	79
5	Conclusions and Outlook	81
	References	85

Introduction

Since R. Feynman's seminal lecture in 1982 [1], several experimental progresses have been achieved to allow the creation of *in vitro* quantum environments which can recreate the physics of other systems in a more controlled way [2]. Ultracold atoms are one of the most promising candidates for the study of open problems related to condensed matter and many-body physics [3].

Ultracold atoms have remarkable properties which distinguish them among all the other systems, such as the possibility of controlling at will most of the experimental parameters such as dimensionality [4, 5], interactions [6, 7] and trapping potentials [8]. Ultracold atoms are almost ideal systems where Hamiltonians can be implemented to study relevant [9] and emergent [10] problems in physics.

The field of quantum simulation with cold atoms was actually triggered by the realization of the superfluid to Mott insulator transition in 2002 [11], and since then many other achievements followed, like the evidence of Anderson localization in disordered lattices [12, 13] or the first experimental observation of the Dicke quantum phase transition in a Bose-Einstein condensate placed in a cavity [14].

Nowadays one of the hottest topics is certainly the physics of strongly correlated fermions in reduced dimensionality, in particular the two dimensional (2D) case. It is believed that this kind of physics lies at the basis of very intriguing systems which, after many years since their discovery, are still a big challenge for theoreticians, like high-Tc superconductors [15] or, more in general, layered Fermi superfluids.

The always more sophisticated techniques of optical manipulation have allowed to first explore the 2D physics in bosonic systems, revealing the signature of exotic phases like the Berezinskii-Kosterlitz-Thouless (BKT) transition [16], and now to address the challenge over unconventional phenomena in the fermionic counterparts [17, 18].

In this Thesis I describe the realization and characterization of a cold sample of fermionic (${}^6\text{Li}$) lithium atoms trapped in a magneto-optical trap (MOT). The fermions are cooled to temperatures of the order of hundreds of micro Kelvin by laser cooling techniques.

This result has been accomplished by setting up a new generation experimental apparatus. In the near future it will be used to produce and to investigate 2D ultracold atomic Fermi gases of ${}^6\text{Li}$. One of the most interesting parts of this setup relies on the possibility of controlling at will the interactions among the atoms through Feshbach resonances [7]. For our goals the most interesting regime is the so-called BEC-BCS crossover [19, 20], which is the transition between a molecular Bose-Einstein condensate (BEC) and a superfluid of Cooper-like pairs described by the Bardeen-Cooper-Schrieffer theory (BCS). In this regime the correlations between particles are no more negligible and many-body effects become predominant. At the crossover the size of these pairs is much smaller than the one of conventional Cooper pairs. It is known [21, 22] that electrons' pairs in high-Tc superconductors are smaller than regular Cooper pairs in type I and type II superconductors. It is believed that there is a strong connection among pairs in high-Tc superconductors and the one at the BEC-BCS crossover in ultracold atomic systems [23].

Moreover, thanks to the possibility of tailoring arbitrary optical potentials, we can engineer 2D Fermi gases in different configurations, ranging from the single layer case, to the two layers one and also to the multi-layer one. The idea is to reconstruct step by step, or better, layer by layer the configuration of a high-Tc superconductor, which is actually a superposition of layered 2D planes. Differently from what can be done in solid state physics, we can shape at will our system to look at the effects of layering on the genesis of superfluidity in this systems. P.W. Anderson suggested that if electrons in cuprates were not described by Fermi liquid theory, an increase of the critical temperature for superfluidity would be possible [24]. However this

statement is quite controversial, since it is still not clear if Fermi liquid theory describes the normal phase of 2D Fermi gases, neither in the single layer nor in the multi-layer case. Because of this, one of the other possible directions of this experiment is studying the thermodynamical equation of state of the 2D Fermi gas, both in the single layer and multi-layer configuration.

Another hallmark of ultracold atoms is the possibility to add controlled disorder by speckle potentials [25]. It is known that superfluidity may be destroyed by disorder. However, in high-Tc superconductors the disorder induced phase transition from a superconducting to an insulating state is still under debate [26].

For all these reasons, ultracold atoms are ideal systems where these open questions may be addressed.

The main features of the new experimental apparatus are described below.

The heart of the apparatus is an ultra-high vacuum system where the degenerate atomic sample is produced and investigated. The main parts of the vacuum system are the oven, where the thermal atomic vapor of lithium 6 is produced, the Zeeman slower, where the first cooling stage is performed, and finally the science chamber, where quantum degeneracy is achieved and the experiments realized. I participated from the beginning in the construction of vacuum system and then in the bake out procedure which was needed to achieve a pressure below 10^{-11} mBar inside the science chamber. Such low pressures are needed to achieve quantum degeneracy in the atomic system.

I've also contributed to mount the optical system and the laser setup, to generate the different laser frequencies needed to cool the atoms.

I've also designed the magnetic coils required for the manipulation of the interactions via magnetic Feshbach resonances [7] and a preliminary project of a microscope objective to observe lithium atoms with high resolution [27].

This Thesis is organized in the following way:

- In chapter 2 we briefly show the theoretical model of the Doppler theory of laser cooling and we give some hints about how atoms can be effectively cooled.

- In chapter 3 the experimental apparatus is described. We describe the main components of the vacuum system used for slowing and cooling the atoms.
- In chapter 4 we present our characterization of the MOT of lithium atoms. We show the dependance of the atom number and temperature of the MOT versus the different parameters of the experiment.

Laser Cooling

In this chapter we will briefly describe the theory behind laser cooling and how it is possible to simultaneously cool and trap an atomic vapor. We will also explain some of the limits of this technique, in particular the ones concerning the lithium case.

2.1 Overview

The controlled transfer of linear momentum from photons to atoms lies at the basis of laser cooling. If an atom in the ground state absorbs one photon of wave vector \vec{k}_L from a laser field, the momentum \vec{P} of the center of mass of the atomic system is changed by an amount $\hbar\vec{k}_L$. The energy scale of the process is called recoil energy and has the form:

$$E_{\text{rec}} = \frac{\hbar^2 k_L^2}{2M} \quad (2.1)$$

where M is the atomic mass.

When the atom is in the excited state, after a typical time $\tau = 1/\Gamma$, where Γ is the natural width of the excited state, the atom goes back into the ground state, spontaneously emitting one photon. The difference between these processes is that the spontaneous emission is isotropic, and the absorption is not (figure 2.1). On average the momentum change due to emission is zero. The atom experiences a force which has opposite direction respect to its velocity. After one cycle of absorption

and emission, the average change in the atom's velocity is:

$$\delta v = \frac{\hbar k_L}{M} \quad (2.2)$$

The order of magnitude of this shift is about few millimeters per second. When

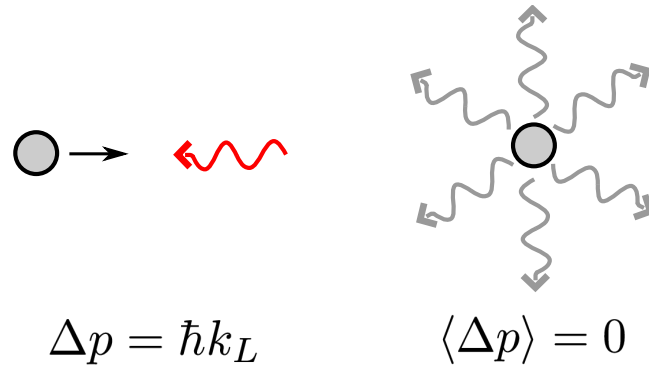


Figure 2.1: Schematic of the cooling mechanism. The absorption process allows to control the direction of recoil, reducing the axial velocity component of the atom, while the emission is isotropic and so the mean momentum variation is zero.

using the D2 line transitions, the variation for ^{87}Rb atoms is approximately $\delta v=5.9$ mm/s, while for ^6Li is about 99 mm/s, because of its smaller mass. Since at room temperature the atoms usually have speed of the order of hundreds of meters per second, a relevant speed reduction would imply an absorption of more or less 10^5 photons by every atom.

In 1975, T. Hansch and A. Schalow [28] proposed the first experimental scheme for cooling an atomic gas, later called optical molasses. In this scheme, the atoms are placed between two counter propagating laser beams, red detuned respect to their atomic transition. The atoms feel more the action of the opposite beam, absorbing more photons from it. This creates a viscous force, which will reduce, thanks to several cycles of absorption and emission, the atomic speed and so the temperature of the gas.

Laser cooling was immediately considered a fascinating technique for laser spectroscopy: obtaining an almost Doppler free atomic sample would have granted an optimal source for high precision spectroscopic measurements. It's only in the early 90's that laser cooling techniques start to be considered as a key ingredient for com-

pleting the long quest for Bose-Einstein Condensation, predicted in 1924 by Bose [29] and never observed till 1995, when E. Cornell and collaborators [30] achieved it in an dilute atomic gas of rubidium atoms (^{87}Rb), thanks to the mastering of both laser cooling and evaporative cooling techniques [31]. The continuous development of those techniques brought the D. Jin's group to realize just three years later the first degenerate fermionic atomic vapor in a sample of potassium ^{40}K [32].

In the following part of this chapter we briefly explain the theoretical model to derive the expression of the force a laser beam can exert on a two level atom system. We will see that this force has two components, one dissipative, used for cooling and another conservative, useful for trapping and manipulating the atoms.

2.2 The radiative force

Our system is composed by a two level atom immersed in a monochromatic laser field. The atom's levels, indicated as $|g\rangle$ for the ground state and $|e\rangle$ for the excited, are separated in energy by $\hbar\omega_A$. The laser field has an energy of $\hbar\omega_L$ per photon and its electric field \vec{E}_L can be expressed as:

$$\vec{E}_L(\vec{R}, t) = \vec{\epsilon}(\vec{R})\mathcal{E}_L(\vec{R})\cos(\omega_L t + \phi) \quad (2.3)$$

where $\vec{\epsilon}$ is the polarization vector and $\mathcal{E}_L(\vec{R})$ the amplitude of the field in \vec{R} . The frequency difference $\delta_0 = \omega_L - \omega_A$ among the laser beam and the atomic transition is called detuning.

The dipole moment of the atom is coupled both to the laser field and to the empty modes of the electromagnetic vacuum field. Because of this last coupling term, excited states are not stable and the spontaneous emission happens.

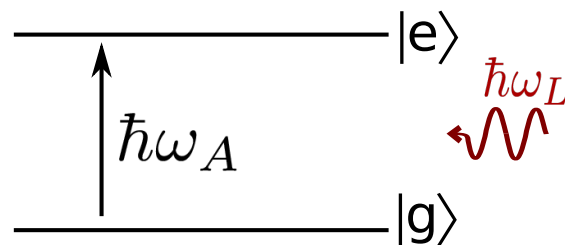


Figure 2.2: Two level atom system coupled to an external laser field.

The atom-laser coupling term \hat{V}_{AL} has the form:

$$\hat{V}_{AL} = -\vec{d} \cdot \vec{E}_L \quad (2.4)$$

which in the Rotating Wave Approximation (RWA) can be written considering only the quasi-resonant terms as:

$$\hat{V}_{AL} = \frac{\hbar\Omega(\vec{R})}{2} \left[e^{-i\phi(\vec{R}) - iw_L t} |e\rangle\langle g| + h.c. \right] \quad (2.5)$$

where Ω is the Rabi frequency.

The equations of motion can be developed in a semi-classical way. The assumption of an atomic wave packet localized both in coordinate ($\Delta x \ll \lambda_L$) and in momentum space ($\Delta p/m \ll \lambda_L \Gamma$) gives us the relation:

$$m\Gamma/k_L^2 \gg \hbar/2 \quad (2.6)$$

which can be arranged in the following way:

$$T_{\text{ext}} = \frac{\hbar}{E_{\text{rec}}} \gg \frac{1}{\Gamma} = T_{\text{int}} \quad (2.7)$$

The terms T_{ext} and T_{int} set the timescale of the external and internal degrees of freedom, respectively, of the atom. T_{ext} represents the time while atom and laser keep on interacting before the Doppler shift breaks the resonance condition. T_{int} represents the lifetime of the excited state. The internal degrees of freedom evolve much faster than the external ones, so that the atomic wave packet will be still localized after one cycle of absorption and emission.

The quantum mechanical operators of the position and momentum of the atom can so be treated as classical variables \vec{r} and \vec{p} , and an expression for the light-induced force can be written as:

$$\vec{F} = -\vec{\nabla} \hat{V}_{AL} - \vec{\nabla} \hat{V}_{AV} \quad (2.8)$$

where \hat{V}_{AV} is the atom-vacuum coupling operator.

Considering the mean value of eq.(2.8), we can neglect the \hat{V}_{AV} operator, since spontaneous emission is random and isotropic and on average is zero. The mean force

$\vec{\mathcal{F}}$ has now the form:

$$\vec{\mathcal{F}} = \langle \hat{\vec{F}} \rangle = -\langle \vec{\nabla} \hat{V}_{AL} \rangle = Tr(\hat{\sigma} \vec{\nabla} \hat{V}_{AL}) \quad (2.9)$$

where $\hat{\sigma}$ is the density matrix operator.

The entries of the density matrix are coupled by a set of differential equations, usually called Optical Bloch Equations (OBE). By solving the OBE in the steady-state case ($\frac{d\sigma}{dt} = 0$) for an atom at rest, eq.(2.9) can be written as:

$$\vec{\mathcal{F}} = -\hbar\Omega(\vec{r})(u_{st}\alpha(\vec{r}) + v_{st}\beta(\vec{r})) \quad (2.10)$$

with $\alpha = \frac{\vec{\nabla}\Omega(\vec{r})}{\Omega(\vec{r})}$ and $\beta = \vec{\nabla}\phi(\vec{r})$.

The terms u_{st} and v_{st} are the steady-state solutions of the OBE and can be expressed as:

$$\begin{aligned} u_{st} &= \frac{\delta_0}{\Omega} \frac{s}{1+s} \\ v_{st} &= \frac{\Gamma}{2\Omega} \frac{s}{1+s} \end{aligned} \quad (2.11)$$

where s is the saturation parameter and has the form:

$$s = \frac{\Omega^2/2}{\delta_0^2 + \Gamma^2/4} \quad (2.12)$$

A more detailed solution of this problem can be found in [33].

To better understand the role of these solution, it is useful to look at the mean value of the electric dipole operator:

$$\langle \hat{\vec{d}}_{st} \rangle = Tr(\hat{\sigma} \hat{\vec{d}}) = \vec{d}(u_{st} \cos(\omega_L t + \phi) - v_{st} \sin(\omega_L t + \phi)) \quad (2.13)$$

We see that the components u_{st} and v_{st} are proportional to the in-phase and quadrature components respectively of the dipole operator. The term of the radial force proportional to u_{st} is so a conservative one while the one proportional to v_{st} is a dissipative one. In eq.(2.10), the term proportional to the gradient of the Rabi frequency and to u_{st} is called *dipole force*, while the one proportional to the gradient of the phase and to v_{st} is called *radiative pressure*. The solution of eq.(2.13) tells

us that the dipole force is conservative while the other is dissipative. Moreover the dipole force is due to stimulated processes while the other to spontaneous emission. Their features will be described in the following paragraphs.

2.2.1 Radiative pressure and dipole force

We can apply our results to the very simple case of an incident plane wave, which has an electric field of the form:

$$\vec{E} = \vec{e} \mathcal{E}_L \cos(\omega_L t - \vec{k}_L \cdot \vec{r}) \quad (2.14)$$

Since the amplitude of the field \mathcal{E}_L is uniform, the gradient of the Rabi frequency is zero and the dipole force too. The gradient of the phase is $\vec{\nabla} \phi = -\vec{k}_L$ and the radiative pressure becomes:

$$\vec{\mathcal{F}}_{\text{rad}} = \hbar \vec{k}_L \frac{\Gamma}{2} \frac{s}{1+s} \quad (2.15)$$

or in an equivalent way:

$$\vec{\mathcal{F}}_{\text{rad}} = \hbar \vec{k}_L \frac{\Gamma}{2} \frac{\Omega^2/2}{\delta_0^2 + \Omega^2/2 + \Gamma^2/4} \quad (2.16)$$

As the plane wave, the force is opposite respect to the atom's direction. When the laser saturates the transition ($s \rightarrow \infty$), the force reaches its maximum value $\mathcal{F}_{\text{MAX}} = \hbar k_L \frac{\Gamma}{2}$. For the ${}^6\text{Li}$ case this corresponds in having a maximum acceleration of the order of $a_{\text{MAX}} \simeq 10^6 g$, where g is the gravitational acceleration. The equation (2.15) tells us that the force is equal to the transferred momentum $\hbar \vec{k}_L$ of a single photon times the average number of photons absorbed per second, which in a two level system is just $\frac{\Gamma}{2} \frac{s}{1+s}$.

The addition of a second identical plane wave, counter propagating respect to the previous one, will create a standing wave with electric field

$$\vec{E}_L = \vec{e} \mathcal{E}_0 \cos(k_L x) \cos(\omega_L t) \quad (2.17)$$

whose amplitude, equal to $\mathcal{E}_0 \cos(k_L x)$ isn't uniform anymore, while the phase is zero. The gradient of the Rabi frequency is no more null and neither the dipole force.

As previously said, the dipole force arises from the stimulated emission process. We

can imagine that the atom absorbs one photon, for example with wave vector \vec{k}_L and then it emits another one with wave vector $-\vec{k}_L$ by stimulated emission in the other laser field.

The dipole force can be written now as:

$$\vec{\mathcal{F}}_{\text{dip}} = -\frac{\hbar\delta_0}{4} \frac{\vec{\nabla}\Omega^2}{\delta_0^2 + (\Gamma^2/4) + (\Omega^2/2)} = -\vec{\nabla}U \quad (2.18)$$

where $U = \frac{\hbar\delta_0}{2} \ln\left(1 + \frac{\Omega^2/2}{(\Gamma^2/4) + \delta_0}\right)$. We see that the dipole force is a conservative one. We can also notice that both the force and the potential depend linearly on the detuning δ_0 : in the red detuning case ($\delta_0 < 0$), we have a negative potential energy and so a trapping potential, otherwise in the blue detuning case, ($\delta_0 > 0$), the potential becomes repulsive.

2.2.2 Force on a moving atom

We will now extend the results from the previous section to the case of a moving atom, but the treatment won't be very different from the previous one. Having assumed $T_{\text{ext}} \ll T_{\text{int}}$, we can neglect the variation of the atom velocity during the timescale of the internal variables: the velocity is assumed constant for the calculation of the force. The only relevant change we have to make is in the detuning expression, since the Doppler effect needs to be taken into account. The laser electromagnetic wave with frequency ω and wave vector \vec{k}_L will have frequency $\omega - \vec{k}_L \cdot \vec{v}$ in the atom's frame, where \vec{v} is the velocity of the atom itself. In the case of the incident plane wave we can write the same expression for the force as in (2.15), just with the addition of the Doppler effect:

$$\vec{\mathcal{F}}_{\text{rad}} = \hbar\vec{k}_L\Gamma \frac{\Omega^2/4}{(\omega_L + k_L v - \omega_A)^2 + (\Gamma^2/4) + (\Omega^2/2)} \quad (2.19)$$

It is more convenient to introduce the substitution $\Omega = \Gamma\sqrt{\frac{I}{2I_s}}$, where I is the intensity of the beam and I_s the saturation intensity of the atomic system. The expression (2.19) now reads as:

$$\vec{\mathcal{F}}_{\text{rad}} = \hbar\vec{k}_L \frac{\Gamma}{2} \frac{I/I_s}{1 + I/I_s + (2(\delta_0 + k_L v)/\Gamma)^2} \quad (2.20)$$

The behavior of this force is reported in figure 2.3. The force is maximum at the condition of zero effective detuning $\delta = \delta_0 + k_L v$ and has a Lorentzian shape for small intensities. When the laser intensity is raised, the force broadens and saturates for all the velocity classes at the value \mathcal{F}_{MAX} .

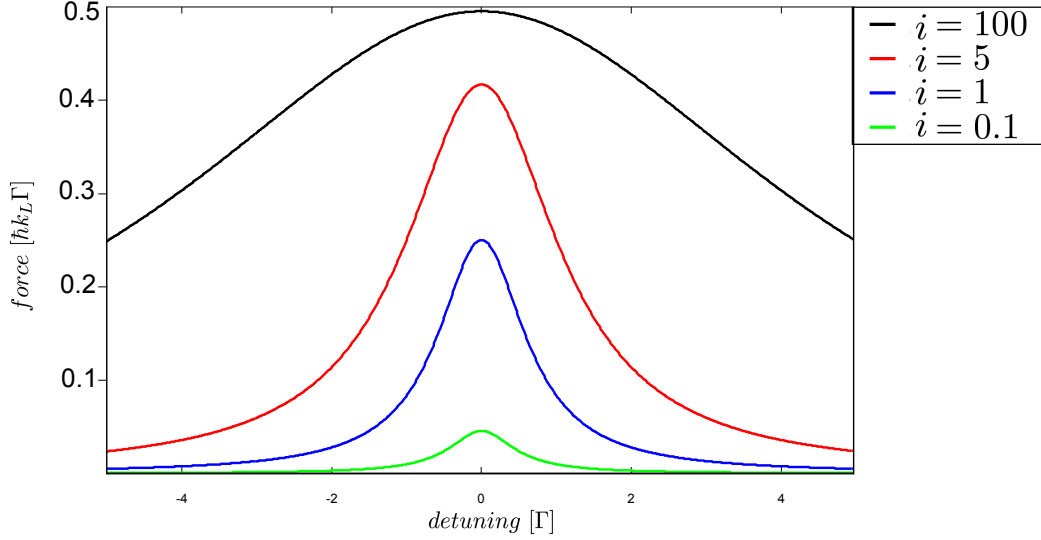


Figure 2.3: Behavior of the dissipative component of the radial force in function of the detuning $\delta = \delta_0 + k_L v$, at different intensities $i = I/I_s$. The detuning is expressed in unities of Γ , while the force in unities of $\hbar k_L \Gamma$. The force is maximum when the Doppler shift compensate for the difference among the laser frequency and the atomic transition ($\delta = 0$). At small intensities the force has a Lorentzian shape while at higher intensities the force broadens over different velocity classes.

2.3 Optical Molasses

In order to create a viscous force, T. Hansch and A. Schalow [28] proposed to combine two red detuned plane wave with opposite wave vectors. The forces created by the two beam can be written as:

$$\vec{\mathcal{F}}_{\text{rad}}^{\pm} = \pm \hbar \vec{k}_L \frac{\Gamma}{2} \frac{I/I_s}{1 + I/I_s + (2(\delta_0 \pm k_L v)/\Gamma)^2} \quad (2.21)$$

where the *plus* sign indicates the wave propagating against the atom, and the *minus* sign the one with the same direction of the atom.

In the case of no interference among the beams, they can be considered as acting independently on the atom. The total force is just the sum of the two forces of eq.(2.21), which in the limit of small velocities and intensities has the form:

$$\vec{\mathcal{F}}_{\text{rad}}^{\text{tot}} = \hbar \vec{k}_L \frac{\Gamma I}{2 I_s} \frac{16 k_L v (-\delta_0) / \Gamma^2}{1 + \frac{8}{\Gamma^2} (\delta_0^2 + k_L^2 v^2) + \frac{16}{\Gamma^4} (\delta_0^2 - k_L^2 v^2)^2} \quad (2.22)$$

The force is linear in the detuning, which controls the direction of it. In the case of red detuning, the force has the same direction of the laser beam going against the atom. In figure 2.4 the behavior of this force is reported in function of $k_L v$.

Considering the case of small velocities around $v = 0$, and assuming $|k_L v| \ll \delta_0$

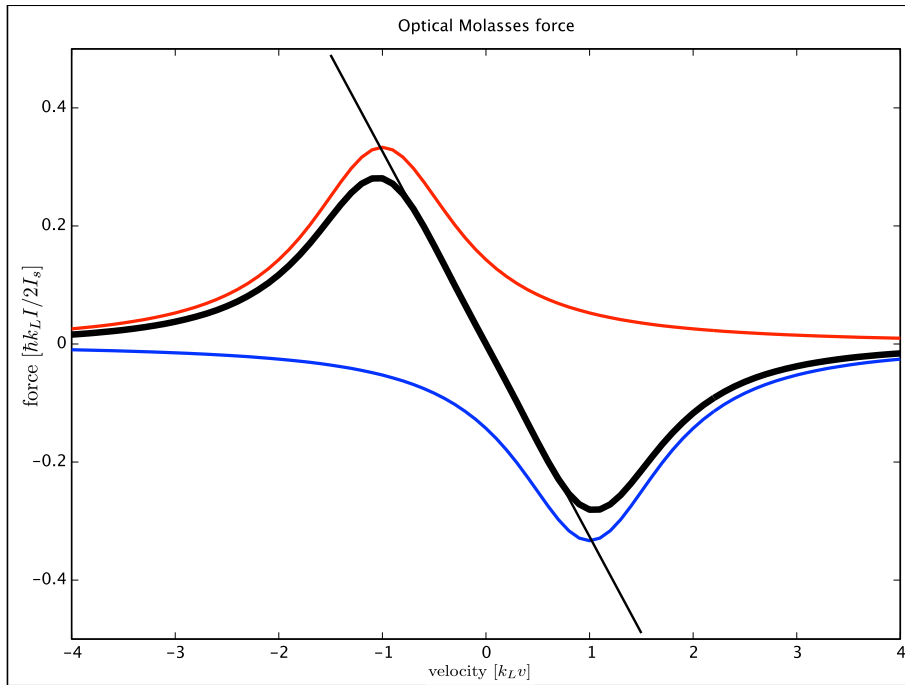


Figure 2.4: Behavior of the radial force of a molasses. The blue and the red lines are the forces of the single beams. The black one is their combined action. For small velocities the slope of the curve is linear and negative, as a typical viscous force. Arbitrary values have been set for the parameters as: $|\delta_0| = \Gamma = 1$ MHz.

and $|k_L v| \ll \Gamma$, the expression (2.22) reads as:

$$\vec{\mathcal{F}}_{\text{rad}}^{\text{tot}} = 4 \hbar k_L^2 \frac{I}{I_s} \frac{2 \delta_0 / \Gamma}{(1 + (2 \delta_0 / \Gamma)^2)^2} \vec{v} \quad (2.23)$$

We see that, if $\delta_0 < 0$, the radial force assumes the typical expression of a viscous force: $\vec{\mathcal{F}}_{\text{rad T}} = -\alpha\vec{v}$, with α positive and equal to:

$$\alpha = 4\hbar k_L^2 \frac{I}{I_s} \frac{2|\delta_0|/\Gamma}{(1 + (2\delta_0/\Gamma)^2)^2} \quad (2.24)$$

The Doppler effect makes the atom more resonant with the counter propagating one, forcing it to scatter more backwards than forward.

2.3.1 Cooling Limit

Light beams can be used to slow atoms down with a consequent reduction of the temperature of the atomic system. But there is a limit temperature that can be reached. First of all we have to consider that photons act more or less as a thermal bath and so atoms cannot have an energy lower than the one of the photons. Even if the mean value of the spontaneous process is zero, each atom after spontaneously emitting acquires a random momentum $\hbar k_L$ which can increase its energy, so raising the temperature of the system. We can roughly define a minimum temperature:

$$T_{\text{rec}} = \frac{E_{\text{rec}}}{k_b} \quad (2.25)$$

which represents a lower bound to our cooling technique.

What actually happens is that the random recoil of the atom due to the spontaneous emission forces the atom itself to perform a random walk of step size $\hbar k_L$ in momentum space. This induces a heating mechanism which reduces the cooling effect of the molasses.

When equilibrium among the opposing effects is reached, the temperature of the system can be expressed as:

$$k_b T = \frac{\hbar\Gamma}{4} \frac{1 + (2\delta_0/\Gamma)^2}{2|\delta_0|/\Gamma} \quad (2.26)$$

which for $\delta_0 = -\Gamma/2$ has a minimum temperature:

$$k_b T_{\text{min}} = \hbar \frac{\Gamma}{2} \quad (2.27)$$

This limit temperature is usually called Doppler temperature, and in the case of ${}^6\text{Li}$ it's of the order of $140\mu\text{K}$.

2.4 The Magneto-Optical Trap

Since the force in a molasses is just a viscous one, atoms cannot be trapped in it. After some time spent in the molasses any atom will escape from it. This can also be seen as a consequence of the optical Earnshaw theorem which claims that the only radiative pressure cannot be used in order to create a minimum of potential energy where neutral atoms could be trapped.

After J. Dalibard's proposal in 1986, D. Pritchard and collaborators [34] succeeded in trapping a relevant amount of cold atoms. Their solution relied on the addition of a magnetic field gradient to two counter propagating beams with opposite circular polarizations. This configuration is nowadays called Magneto-Optical Trap (MOT) and from the very beginning has been considered as the starting point for ultracold atoms experiments.

2.4.1 MOT Doppler Theory

In the simple one-dimensional case, the MOT configuration consists of two counter propagating red detuned laser beams with opposite circular polarization, namely σ^+ and σ^- , with the addition of an inhomogeneous magnetic field. The field magnitude is zero in the center of the trap and increases linearly along the direction of propagation of the beams. This position dependent Zeeman effect will affect the force acting on the atoms. The example of this scheme for an atom with ground state with $F = 0$ and excited one with $F' = 1$ is reported in figure 2.5. If the field has the form $\vec{B} = b\vec{z}$, the hyperfine energy levels of the atom will be shifted by an amount $\Delta E = \mu'bz$ due to the Zeeman effect, with $\mu' = \mu_B g_{F'} m_{F'}$. The presence of the circular polarization will cause the atom to interact more with the beam pushing it towards the center of the trap and the red detuning of the beams will cool the atom at the same time.

In (2.21) we have now to consider the shifts caused by the Zeeman effect in the detuning:

$$\vec{\mathcal{F}}_{\text{rad}}^{\pm} = \pm \hbar \vec{k}_L \frac{\Gamma}{2} \frac{I/I_s}{1 + I/I_s + (2(\delta_0 \pm (k_L v + \frac{\mu'bz}{\hbar}))/\Gamma)^2} \quad (2.28)$$

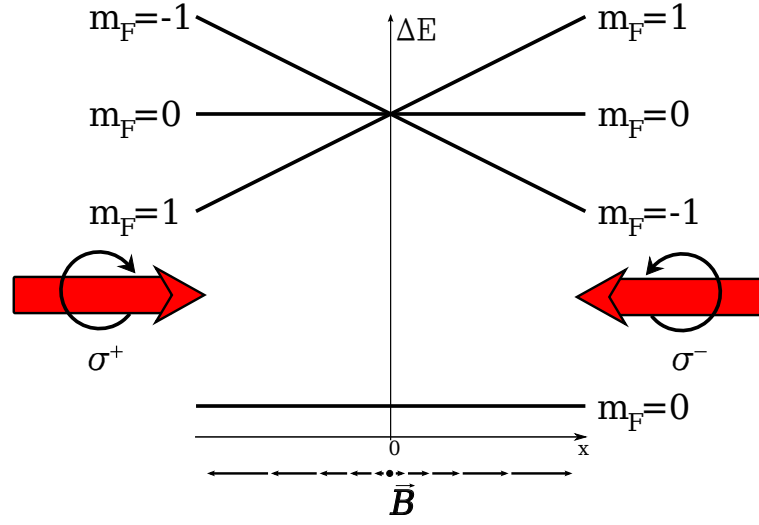


Figure 2.5: Scheme of the MOT. The addition of circular polarization to the beams makes the atoms more interacting with the counter propagating one, as if there were a restoring force towards the center of the trap.

Considering the limits $k_L v \ll \delta_0$ and $\Delta E/\hbar \ll \delta_0$, the global force of the two beams becomes:

$$\vec{\mathcal{F}}_{\text{rad T}} = 4\hbar k_L \frac{I}{I_s} \frac{2\delta_0/\Gamma}{(1 + (2\delta_0/\Gamma)^2)^2} \left(\vec{v} + \frac{\mu' b \vec{z}}{\hbar} \right) \quad (2.29)$$

which can be written as:

$$\vec{\mathcal{F}}_{\text{rad T}} = -\alpha \vec{v} - K \vec{z} \quad (2.30)$$

where we have set:

$$K = \frac{\mu' b}{\hbar k_L} \alpha \quad (2.31)$$

In the red detuning case, both α and K are positive and eq.(2.30) can be seen as the one of a damped harmonic oscillator. We can write the differential equation of the atomic motion as:

$$\ddot{z} + \gamma \dot{z} + w_{\text{trap}}^2 z = 0 \quad (2.32)$$

where we have set $\gamma = \frac{\alpha}{M}$ and $w_{\text{trap}}^2 = \frac{K}{M}$.

An efficient trapping is achieved when the overdamping condition, namely $\zeta = \frac{\gamma}{2w_{\text{trap}}} > 1$, is satisfied. In this way atoms are simultaneously cooled and confined in a region of space around the center of the trap.

2.4.2 The capture range and velocity

The capture range r_C is the maximum distance an atom can have from the MOT center to be trapped, while the capture velocity v_C is the analogous for the atom's velocity.

The capture radius can be approximated as the point where an atom at rest is in resonance with the pushing back MOT beam, and so

$$r_C = \frac{\delta_0 \hbar}{\mu' b} \quad (2.33)$$

The capture velocity is the maximum velocity an atom can have in order to be effectively trapped by the MOT, if it travels across the entire length of the trap which is indicated as $2r$, where r is the radius of the laser beams.

To estimate the capture velocity, we first look at the position-velocity phase diagram. The confining force has two maxima along these two lines:

$$\begin{aligned} \delta_0 + k_L v + \frac{\mu' b z}{\hbar} &= 0 \\ \delta_0 - k_L v - \frac{\mu' b z}{\hbar} &= 0 \end{aligned} \quad (2.34)$$

In the small intensities limit, we can assume that the force quickly decreases moving away from the position of zero effective detuning, so the atoms that in the coordinate system (z, v) lie outside the region between the two lines of eqs.(2.34) have low probability of getting trapped, unlike the ones in the inside. We may say that the trapped atoms have initial conditions so that the absolute value of the derivative of their velocity respect to the position is equal to or greater than the slope of the two lines of eqs.(2.34), which can be written as:

$$\left| \frac{dv}{dz} \right|_{\text{atom}} \geq \left| \frac{dv}{dz} \right|_{\text{line}} = \frac{\mu' b}{\hbar k_L} \quad (2.35)$$

The critical condition is reached when the relation in (2.35) turns into an equality. Considering $\frac{dv}{dx} = \frac{dv}{dt} \frac{dt}{dz} = \frac{F}{Mv}$, the expression for the critical velocity v_c becomes:

$$v_c = \frac{\hbar k_L F}{\mu' b M} = \frac{\hbar^2 k_L^2 \Gamma}{\mu' b 2M} \frac{s}{1+s} \quad (2.36)$$

The value for the magnetic field gradient is found imposing a resonance condition among the beam and an atom at rest at a distance r from the center:

$$b = \frac{\hbar|\delta_0|}{\mu'r} \quad (2.37)$$

MOT's beams usually have a radius of the order of half inch, because of the limitations due to lenses and mirrors. We decided to perform a simulation of the dynamics of the atoms in the MOT to find reasonable values for experimental parameters. Usually MOT's beams have a detuning of the order of $-2 \sim 3\Gamma$, but to enlarge the area among the two lines of eq.(2.34), we set the value of the detuning at $\delta_0 = -6\Gamma$. From eq.(2.37) we found a magnetic field gradient of about 25 Gauss/cm. The plots of the trajectories in the phase space diagram, with different intensity conditions, are reported in figure 2.6. The two plots represent the dynamics in a MOT for different values of the intensities: on the top $s = 0.1$ and $\zeta \sim 0.2$, on the bottom $s = 2$, and $\zeta \sim 1$. In the small intensities case the atom perform a sort of whirlpool-like motion because of the small damping, while in the other are immediately sucked into the center. When s is raised, also atoms starting from outside the red lines (condition from eq.(2.34)) are trapped, because of the broadening of the force (paragraph 2.2.2). The capture velocities is 60 m/s in the small intensities case while around 250 m/s in the large intensities one. If in the left picture this critical condition is well satisfied, in the large intensities limit atoms with velocities above 80 m/s are not trapped. This is due to the reduced size of the MOT beams, which is only one inch in diameter, preventing the configuration to be effective also for those velocities.

This theory describes the interactions among a laser field and a two-level atomic system. However, it describes well also the case of laser cooling of real multilevel atom. As we will see later, the experimental results we obtained are in good agreement with the ones of the theoretical calculation developed in this chapter.

2.5 Sub Doppler cooling

The theory developed before deals essentially with one dimensional cases and two level atom system, but it is quite obvious that real systems work differently. Moreover experiments performed for the realization of molasses and MOTs usu-

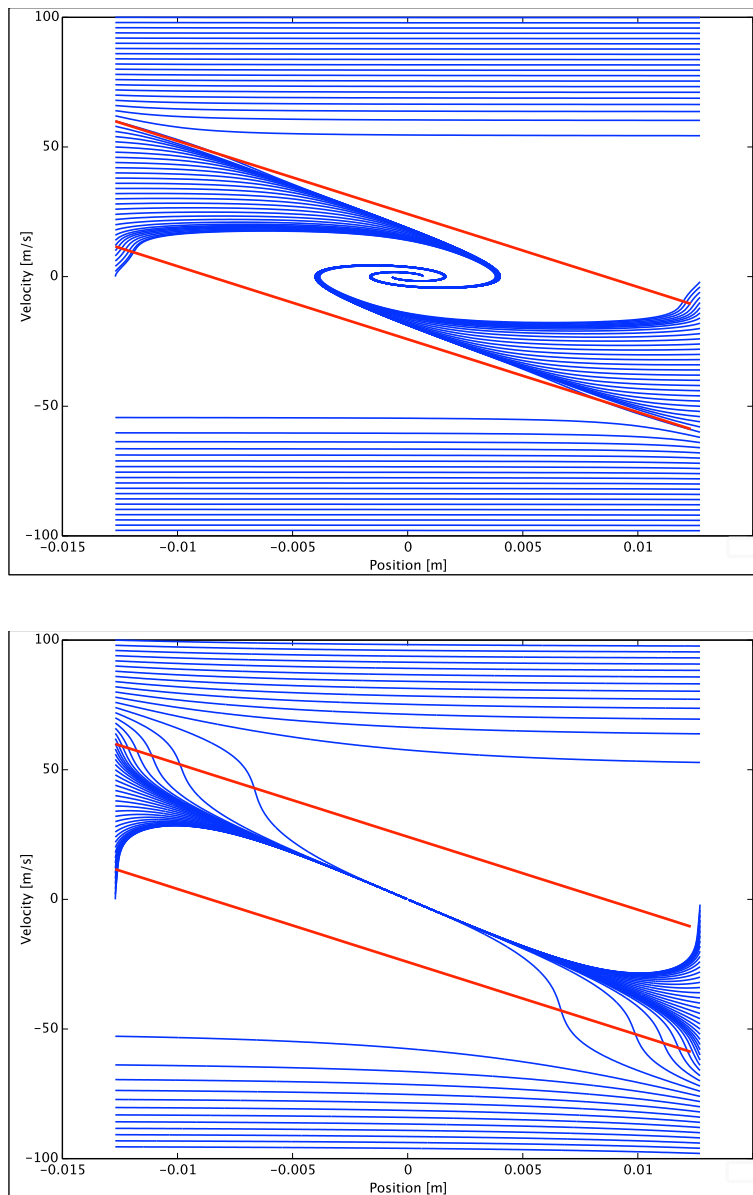


Figure 2.6: Dynamics of the MOT for the small intensities regime (top) and for the large intensities one. The key parameter in the description of the MOT dynamics is the damping term $\zeta = \frac{\alpha}{2\sqrt{mK}}$: $\zeta > 1$ means overdamped motion, while $0 < \zeta < 1$ means just damped.

ally require large intensities for the laser beams, quite above the saturation threshold, and in this case interference effects cannot be neglected.

But just after the Dalibard's proposal, several experiments reported the achievement of temperatures well below the Doppler one. In 1988, in one of the first experiments on the sodium molasses, W. Phillips and collaborators [35] registered a temperature of $40 \mu\text{K}$ while the expected one was of the order of $240 \mu\text{K}$. The theoretical explanation of this phenomenon, mainly achieved by C. Cohen-Tannoudji, relies on the presence of a polarization gradient due to the interference of the beams. From the interplay between this polarization gradient and the hyperfine splitting of the atom, a spatially dependent optical pumping scheme arises. With a naive picture, the optical pumping forces the atoms to occupy the hyperfine level with lowest energy, which is different from point to point because of the polarization gradient. When moving away from a local minimum, the atom, before stopping and inverting its motion, is optically pumped to another minimum and so forced to burn its remaining kinetic energy.

This scheme is called Sub-Doppler cooling and allows to reach temperatures far below the Doppler one. However, the Sub-Doppler theory is valid until temperatures of the order of the recoil energy of the photon are reached, since below this point the semi-classical treatment stops to be valid.

For the lithium case, when cooling using the D2 line transition (paragraph 3.1), the Sub-Doppler cooling is not efficient and a temperature below the Doppler one cannot be reached. This is due to the small energy separation of the levels of the excited state, which doesn't allow to have any close transition. The optical pumping scheme is so inefficient and consequently the whole sub-Doppler mechanism fails.

A typical value of the temperature in a lithium MOT is of the order of 1-2 mK, while the expected temperature is around $140 \mu\text{K}$. However it is possible to reduce this temperature using the so-called compressed MOT stage (CMOT). In the CMOT, after having load a sufficient amount of atoms into the MOT, the repumper intensity is reduced, typically around 1-2% of the initial value and the gradient of the MOT magnetic field increased. After a short period of time, all the atoms fall into a dark state and so they do not scatter anymore with the photons of the cooling beams. In this way the heating effect is reduced. The CMOT stage works for a limited amount of time, since atoms will escape from the trap if no laser beam acts on them. By the way, with this trick it is possible to achieve temperatures around $300 \mu\text{K}$, making

the following dipole trap loading much easier.

By the way, recent advances in laser technology have allowed to succeed in the realization of a MOT using the $2S_{1/2} \rightarrow 3P_{3/2}$ transition at 323 nm (XUV range). Because of its more narrow linewidth ($\Gamma = 2\pi \cdot 159$ KHz), a final temperature of 59 μ K was achieved [36].

Experimental apparatus

In this chapter we will show the experimental apparatus developed and built for the realization of a cold sample of fermionic lithium atoms.

First we explain the properties of the atomic species we decided to cool down and then we describe the real experimental setup which is composed by two complementary parts. The first part is the optical system composed by the laser sources and the optical elements used to manipulate the laser light. The second one is an ultra-high vacuum system, composed by an oven, where the atomic vapor is originally produced, by the differential pumping system, by a Zeeman slower, which represents the first step of the cooling scheme, and by a science chamber, where the last steps of the cooling procedure are done and where all the relevant physics experiments will be performed.

3.1 Lithium 6

The atomic species we use in our experiment is the fermionic isotope of alkali lithium (Li), ${}^6\text{Li}$. With just one s-electron in the outer shell, we have $\vec{S} = \frac{1}{2}$ and $\vec{L} = 0$. The nuclear angular momentum is $\vec{I} = 1$ and so the vector $\vec{F} = \vec{L} + \vec{S} + \vec{I}$, which gives origin to the hyperfine structure, will just have half integer values, justifying the fermionic character of the isotope. However it is also common to distinguish the different transitions only by their $\vec{J} = \vec{L} + \vec{S}$ quantum number. The $2S_{1/2} \rightarrow 2P_{1/2}$ is called the *D1 transition*, while the $2S_{1/2} \rightarrow 2P_{3/2}$ is called the *D2 transition*. We decide to develop our cooling scheme on the D2 line. The advantage respect to the D1 line is that the D2 transition has a lower saturation intensity $I_{sat} = 2.56 \text{ mW/cm}^2$, so that it requires less laser power. Moreover, from a theoretical

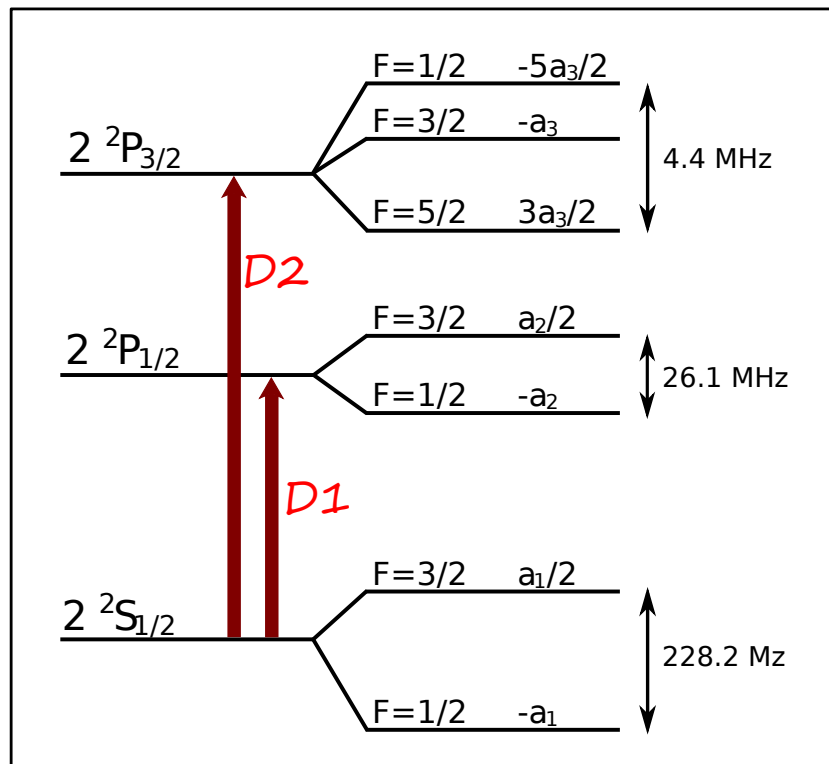


Figure 3.1: Hyperfine structure of ${}^6\text{Li}$ at zero magnetic field. The D1 and D2 transitions are reported. The different a_i coefficients that appear in the figure are the hyperfine constants of the different energy levels.

point of view, the only closed transition in this system is the $F = 3/2 \rightarrow F' = 5/2$ transition contained in the hyperfine structure of the D2 line. However, since the natural linewidth of the transition ($\Gamma/2\pi = 5.9$ MHz) is larger than the hyperfine splitting of the excited state (namely 4.4 MHz), the hyperfine structure cannot be resolved in the absorption spectrum. As a consequence, we can't avoid that some atoms decay into the $F = 1/2$ state of the ground state, whose separation from the $F = 3/2$ is very large instead, i.e. 228 MHz. These atoms are, hence, lost from the cooling cycle and in order to recover them we will need another frequency which should pump the atoms from the $2\ ^2S_{1/2} |F = 1/2\rangle$ state to the excited level. These transitions are respectively called cooling and repumper (figure 3.2). The hyperfine structure of ${}^6\text{Li}$ at zero field is sketched in figure 3.1.

3.1.1 Why lithium?

Lithium is one of the most exploited atomic species to produce quantum degenerate gases and in particular ${}^6\text{Li}$ is one of the only two stable fermionic isotopes in all the alkali elements, the other one being the ${}^{40}\text{K}$. The great interest in using lithium 6 for realizing toy models of condensed matter systems is because of the presence of a broad Feshbach resonance among the two lowest hyperfine levels, which is located at 834 Gauss.

The Feshbach resonance comes from nuclear physics but has become a fundamental ingredient in the ultracold atoms research field. The presence of a Feshbach resonance in an ultracold atomic sample allows to tune the scattering length of the two body scattering process [7, 37]. For example, in the zero magnetic field case, two free atoms can interact through a certain potential called open channel. It may also occur that when those atoms occupy different internal states, their interaction is controlled by a different potential. This potential requires an activation energy that at zero field is higher than the one of the open channel, and so scattering through this potential is forbidden: this is called a closed channel (figure 3.4). But the situation may change if the hyperfine states among the two different channels have a

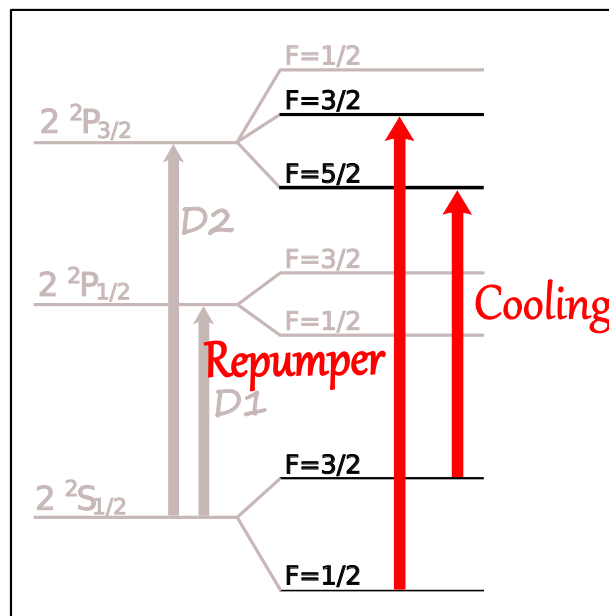


Figure 3.2: Optical transition required in our cooling scheme. The $2\ 2S_{1/2}|F = 3/2\rangle \rightarrow 2\ 2P_{3/2}$ is called cooling. The $2\ 2S_{1/2}|F = 1/2\rangle \rightarrow 2\ 2P_{3/2}$ is called repumper

different magnetic moment. In this way, by applying a magnetic field, we can also change the relative energy among the channels and bring the energy of the closed channel close to or quasi-resonant with the one of the open channel. A Feshbach resonance occurs when the state in the open channel energetically approaches one of the possible bound states of the closed channel. In this way the open channel couples to the closed one and the free atoms "virtually" occupy the bound state. This affects the scattering phase shift and so the real value of the scattering length. The scattering length a in lithium 6 can be tuned ranging from large negative values ($\sim -\infty$) to large positive ones ($\sim +\infty$) as shown in picture 3.4 and its value can be evaluated from the formula:

$$a = a_{\text{bg}} \left(1 + \frac{\Delta B}{B - B_0} \right) \quad (3.1)$$

where a_{bg} is the background scattering length, ΔB is the amplitude of the resonance and B_0 its position. For ${}^6\text{Li}$ we have $a_{\text{bg}} = -1405a_0$ where a_0 is the Bohr radius, $\Delta B = 300$ Gauss and $B_0 = 834$ Gauss.

In this scenario we can identify three different situations (figure 3.3) for our atomic system:

- $a < 0$: Attractive side. The energy of the bound state in the closed channel is above the scattering continuum of the open channel and the atoms virtually occupy the bound state. Through calculations with second order perturbation theory, the hyperfine coupling among the scattering continuum and the closed channel lower the energy of the free atoms. The atoms feel an attractive potential and the scattering length becomes negative. We know that a degenerate Fermi gas (DFG) is unstable towards any attractive interaction (Cooper problem), even infinitely small ones. In this situation Cooper-like pairs form on the edge of the Fermi sphere of the DFG. For this reason this side of the resonance is usually called *BCS side*.
- $a > 0$: Repulsive side. The energy of the bound state is below the open channel and the atoms feel a repulsive potential. However the atoms, due to three body processes, can "physically" occupy the bound state and form stable molecules, called Feshbach molecules. In the three body scattering process, one atom absorbs the binding energy for the molecule creation allowing the

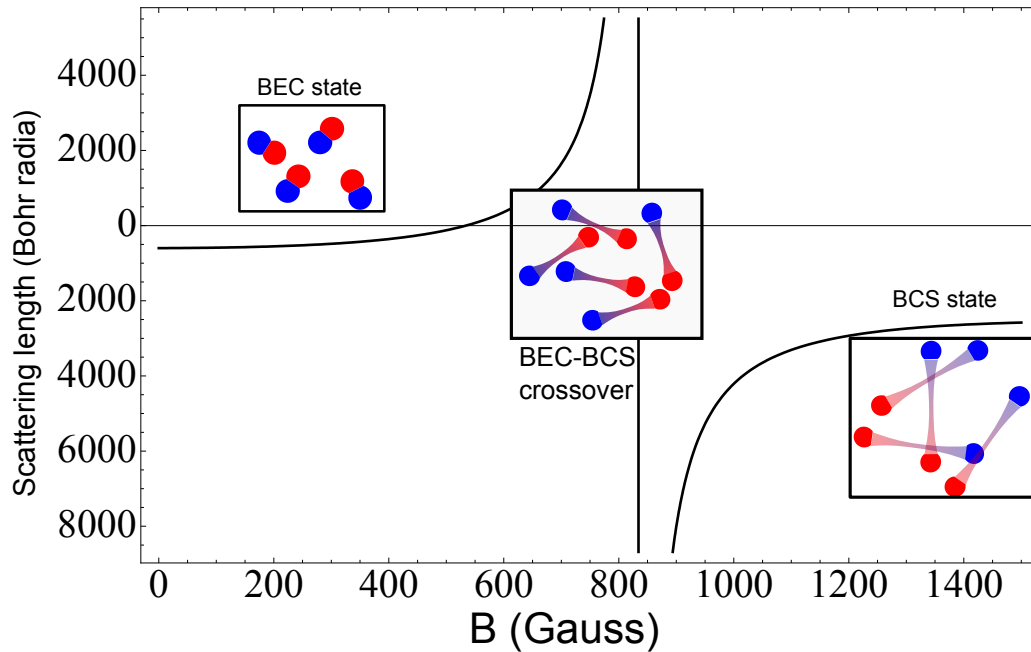


Figure 3.3: Many-body scenario of a DFG of ${}^6\text{Li}$ atoms close to the Feshbach resonance at 834 Gauss.

remaining two to pair up. When we are close to the resonance and a is quite large, these molecules are usually in the highest possible roto-vibrational state among all the possible bound states of the closed channel. Even if they are very large and weakly bound, these molecules last for very long time. Because of their large size, even if the molecules should behave like bosons, the fermionic nature of the two atoms prevails [38]. Pauli exclusion principle acts as a "statistical" shield on these molecules, almost completely suppressing two and three body collisions in the system. On this side of the resonance, the binding energy of the molecules is described by the formula: $E_b = -\frac{\hbar^2}{ma^2}$. This means that when a is large the molecules aren't tight, but when a decreases, so when we go away from the resonance, their binding energy increases and all the molecules get tighter and tighter, increasing more and more their bosonic character. If the temperature is low enough, these fermionic molecules undergo Bose-Einstein Condensation (BEC). This is why this side is called *BEC side*.

However, when tight condensed molecules appear, two and three body losses

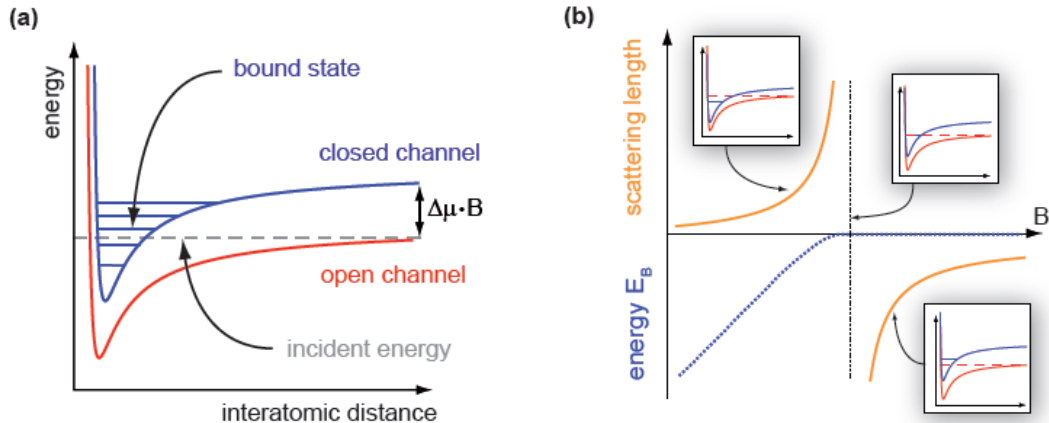


Figure 3.4: a): Elementary way of explaining the concept of closed and open channels. b): Variation of the scattering length and relative position of the closed channel threshold respect to the open channel one. In pale blue the behavior of the binding energy is sketched. On the left this value is quite high and the DFG turns into a BEC. On the BCS side the binding energy of the Cooper-like pairs (BCS gap) decays exponentially. Picture taken from [39].

are no more forbidden by Pauli's principle and consequently the lifetime of the system is extremely decreased. These molecules stay in highly excited states, even if in low roto-vibrational levels. When three body processes happen, two atoms get bounded in the molecular ground state, while the third one absorbs all the large binding energy left behind. This atom with large kinetic energy heats the system up, breaking the quantum degeneracy regime.

- $a = \infty$ Unitary regime. Very close to the Feshbach resonance the scattering length diverges and the DFG becomes strongly interacting. But all the properties of the system can be described by just two parameters: the Fermi energy E_F and the Fermi momentum k_F which set the energy and momentum scales of the whole system respectively. The physical properties of the DFG are said to be universal, which means that they can be found in other different systems such as neutron stars or atomic nuclei. The only different parameter among these systems is their density, which goes from approximately 10^{12} atoms/cm³ in ultracold atomic sample till the huge value of 10^{38} atoms/cm³ in neutron star.

This regime is usually called BEC-BCS crossover since it connects the BEC limit

and the BCS limit across a Feshbach resonance. Despite the divergence of the scattering length the crossover from one side of the resonance to the other one is smooth, and adiabatic switches of the magnetic field value may allow to explore the different regimes during the same experimental cycle.

3.2 Optical system

3.2.1 Laser Sources

As we have seen, two frequency are needed to cool and repump the atoms. Since their difference is around 228 MHz, we can use a single laser source. Our master laser is a Tapered Amplifier High Power Diode Laser produced by TOPTICA. At room temperature and with an injected current of 520 mA, the laser cavity (seed or master oscillator) can produce a beam at 671 nm with a maximum power of 20 mW. Outside the seed two optical isolators are placed. After the isolators, the light has to pass through a Master Oscillator Power Amplifier (MOPA). The MOPA increases the power of the laser light till a maximum value of 400 mW, without changing its wavelength. This whole laser source is placed on an isolated optical table, different from the one where the vacuum system is located. The light for the experiment will be brought from this table to the one of the vacuum system by polarization maintaining optical fibers.

Since in our experiment different wavelengths are needed to efficiently run the slower and the MOT, on the laser table a specific optical path has been realized (figure 3.5) in order to create different beams with the proper value of wavelength and intensity. The changes in frequency are done by making the beams pass through Acousto-Optic Modulators (AOMs). AOMs are devices which contain a quartz crystal connected to a piezo-electric transducer. When oscillating, the transducer creates a sound wave with a tunable frequency which travels inside the quartz. Thanks to photon-phonon interaction, the frequency of the laser wavelength can be changed by an amount equal to the frequency of the oscillating sound wave. Some of the beams have also to pass through an optical amplifier, in order to have their intensity increased. On our table we have put two different optical amplifiers, always produced by TOPTICA, and each one, if injected with 20 mW of laser light at 671 nm, can produce a maximum of 400 mW of laser light at the same wavelength.

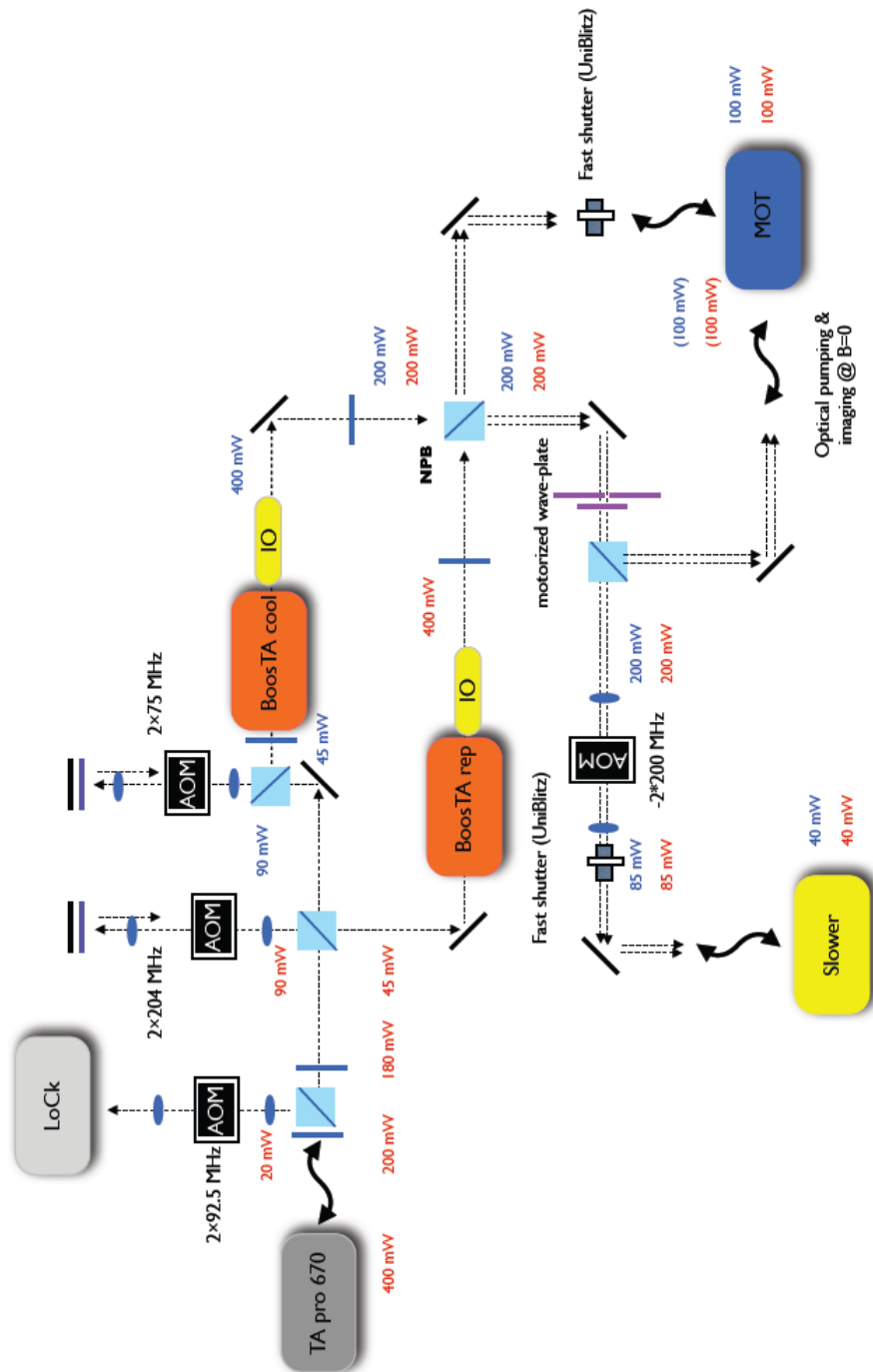


Figure 3.5: Sketch of the optical path realized on the laser table. The values of frequency and power are the ones of the initial theoretical calculation.

3.2.2 Saturated Absorption Spectroscopy Cell

A fundamental element of our apparatus is the cell used to perform Saturated Absorption Spectroscopy (SAS) of the ${}^6\text{Li}$ vapor. SAS is used to lock the laser frequency to an absolute value of reference, which in our case is the D2 line transition in ${}^6\text{Li}$. The cell is placed above the laser's optical table in order to prevent heating of the optical elements placed on it, since the SAS cell has to reach temperature higher than 340°C to efficiently run. The cell is an elongated tube with two windows on the extremities. In the middle there is a cap used to lodge the lithium once put in the cell and a valve which connects the cell to a pre-vacuum system and to an argon reservoir. To load the lithium in the cell, we first put under vacuum the cell with both the scroll pump and the turbo pump of the pre-vacuum system. Then we flux argon inside the cell and, after turning down the turbo pump, we open one of the two windows. The argon pressure has to be high enough in order to feel with bare hands an argon flux coming out from the open window. This helps removing oxygen inside the chamber and in the proximity of the open window. Then we open the lithium beaker and quickly put it inside the chamber in order to prevent oxidation. After closing the windows, we turn on the pumps and later flux some argon in the cell. This time we control the argon flux inside the cell with the help of a metering valve. In this way we can finely tune the argon pressure inside the chamber, avoiding to overload the turbo pump. After reaching an argon pressure of 200 mTorr, we perform for one night the baking of the cell at 200°C to clean both the cell and the lithium sample. The baking is done with the argon valve open and in order to have a constant argon pressure in the cell, which reduces the mean free path of Li atoms, preventing them to stick on the windows. After the baking we reduce the argon pressure inside the cell till a value of 10 mTorr [40]. This value of pressure always prevents lithium to stick on the windows but also minimize the pressure Doppler-broadening of the absorption signal which is checked by shining a single laser beam through the cell, while its frequency is scanned across the atomic transition. After this the cell is closed and detached from the pumps and the argon tank and put on its own table, where it will be thermally isolated from the optical elements next to it (figure 3.6), since for an optimal signal in SAS a temperature of 370°C is required. The description of the SAS techniques and the related signals used to lock the laser is written in the following sections.



Figure 3.6: Picture of the SAS cell on its own optical table. The cell is wrapped with a heating tape and then insulated with fiberglass tape and aluminum foils. Thermal bricks have been put close to it to reduce heating of the optical system.

3.3 Laser Locking

The frequency of a laser light beam can shift and change in time if an accurate locking scheme is not realized. Undesired thermal and current fluctuations happen very frequently during the experiment and can induce a variation of the order of 1 GHz in the laser frequency. For an ultracold sample of atoms this clearly represents a significant problem since the linewidth of the optical transitions is typically of the order of some MHz.

To properly stabilize the laser frequency, we need to observe the absorption spectrum first. In our case we decided to use Saturated Absorption Spectroscopy (SAS) technique to achieve this goal. The key feature in SAS is the absence of the Doppler broadening effect in the absorption line, therefore the exact frequency of the transition can be observed.

3.3.1 Saturated Absorption Spectroscopy

Transition lines in atomic vapors are generally hidden and broadened due to the Doppler effect. Because of this, the narrow Lorentzian profile of any atomic transition will be turned into a large Gaussian one, preventing us from resolving the structure of the atom.

One way to make the transition lines emerge is to use two counter propagating laser beams, called here and after probe and pump beam. The pump beam usually has a larger intensity to saturate the transition. For this reason, this technique is

named Saturated Absorption Spectroscopy (SAS). The two beams cross inside the vapor cell. Any atom, because of the Doppler effect, will see the two beams with different frequency and cannot be in resonance with both of them unless it has zero velocity (figure 3.7). These atoms will be first excited by the pump and then by stimulated emission transferred again into the ground state. This will consequently add a photon to the laser field, increasing the transmitted intensity at this specific frequency.

In our case, instead of having a two level system, we have a three level one, with a two level ground state and one excited level. The transitions from the two different ground states have different energies, namely w_1 and w_2 . In the absorption signal we will see three different dimples. Two of them are due to the resonance of the zero-velocity class at the frequencies w_1 and w_2 . The other one is called cross-over signal and is due to the resonance of a non-zero-velocity class of atoms with both beams (figure 3.8). This can happen if some atoms have velocity \vec{v} such that:

$$\begin{aligned} w_{pu} &= w_L - \vec{k} \cdot \vec{v} = w_1 \\ w_{pr} &= w_L + \vec{k} \cdot \vec{v} = w_2 \end{aligned} \quad (3.2)$$

This means:

$$\vec{k} \cdot \vec{v} = \frac{w_2 - w_1}{2} \quad (3.3)$$

and more importantly:

$$w_L = \frac{w_1 + w_2}{2} \quad (3.4)$$

The atoms will be excited by the pump and then will spontaneously decay into the

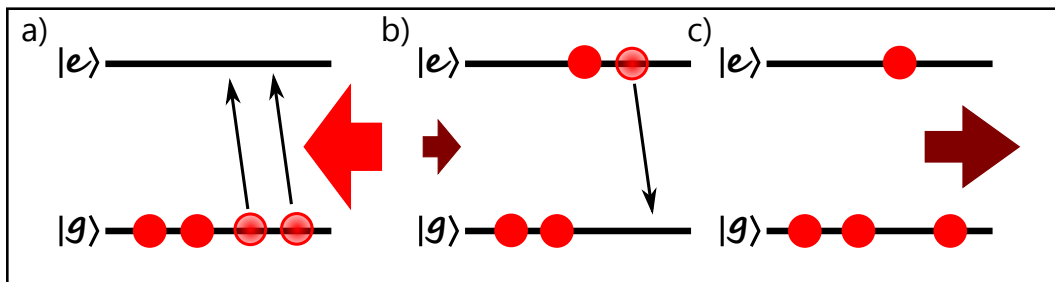


Figure 3.7: Saturated Absorption for the zero velocity class in a two level atom. The pump saturates the transition (a). Because of stimulated emission from the excited level to the ground state (b), the probe intensity is enhanced (c).

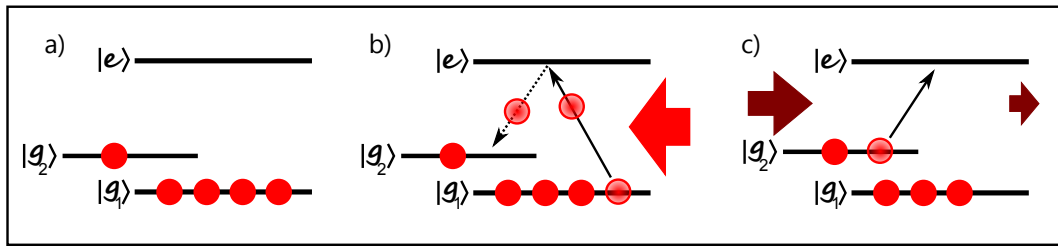


Figure 3.8: Representation of the three levels scheme (a) and absorption process happening when eqs.(3.3) and (3.4) are satisfied. Atoms from the $|g_1\rangle$ ground state are optically pumped by the pump to the $|g_2\rangle$ state (b), or viceversa. The transition of interest to the probe, namely the $|g_2\rangle \rightarrow |e\rangle$, is no more saturated. The outgoing probe beam will have a reduced intensity due to absorption (c).

other ground level. Therefore the transition resonant with the probe will have more atoms to excite. This will induce an enhancement of the absorption and a lowering of the transmitted intensity, as it can be seen in figure 3.9.

The emergence of these sharp dimples is very useful to us, because they create stationary points in the absorption signal which can give us a reference to be exploited in order to lock the frequency through a feedback control system. This will be explained in the following sections.

Frequency Modulation Spectroscopy

Frequency Modulation Spectroscopy (FMS) allows to obtain the derivative of the absorption signal, generally called error signal, which represents the reference for the locking procedure. When scanning through an atomic transition, the addition of controlled time-dependent modulation in the diode current changes the equation for the transmitted intensity I_T as:

$$I_T[v(t)] = I_T[v + m \sin(\omega t)] \quad (3.5)$$

where $m \sin(\omega t)$ is the modulation induced by the diode current, with $m \ll 1$. Assuming the diode current modulation much faster than the one provided by the

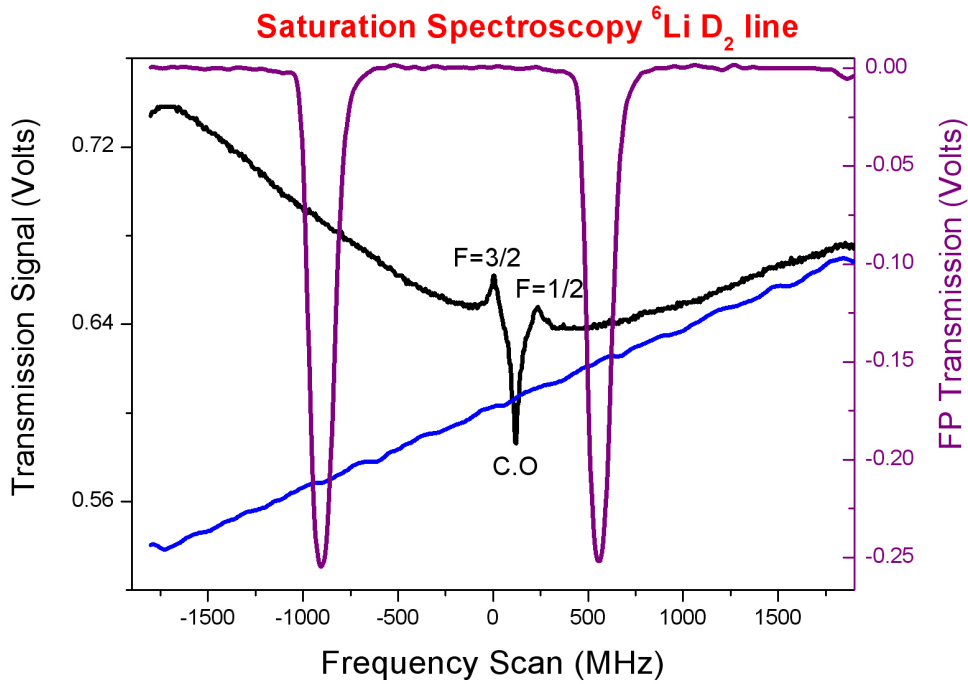


Figure 3.9: SAS signal from the D2 line of ${}^6\text{Li}$ (black line). The blue line represents the piezo modulation and the purple one are the modes of a Fabry-Perot cavity used as reference. These peaks are separated by 1.25 GHz. The black line shows very well the appearance of the Doppler free dimples. Those indicated by $F = 3/2$ and $F = 1/2$ are due to the resonance of the zero velocity class at the exact value of the two atomic transitions. The one indicated by *C.O.* is the cross-over signal. The zero of the x-axis is set at the frequency of $F=3/2$. Thanks to the reference of the Fabry-Perot we could effectively check that the separation among the $F=3/2$ and the $F=1/2$ state is 228 MHz.

piezo scan, with some trigonometric trick, eq.(3.5) can be written as:

$$I_T[v(t)] = \left(I_T + \frac{m^2}{2} \frac{d^2 I_T}{dv^2} + \dots \right) + \sin(\omega t) \left(m \frac{dI_T}{dv} + \frac{m^3}{8} \frac{d^3 I_T}{dv^3} + \dots \right) + \cos(2\omega t) \left(\frac{m^2}{4} \frac{d^2 I_T}{dv^2} + \dots \right) \quad (3.6)$$

This is actually a sum of a constant term (DC term) with an infinite amount of AC terms which oscillate at integer multiples of the frequency of the diode current

modulation.

Using a lock-in amplifier, we can perform phase-sensitive detection at a frequency equal to ω , and isolate only the component oscillating at that frequency. Since m is small, we find that the amplitude of this oscillation is proportional to the derivative of the absorption signal (figure 3.10).

The zero crossing of the derivative at the atomic transition is a good reference, but it

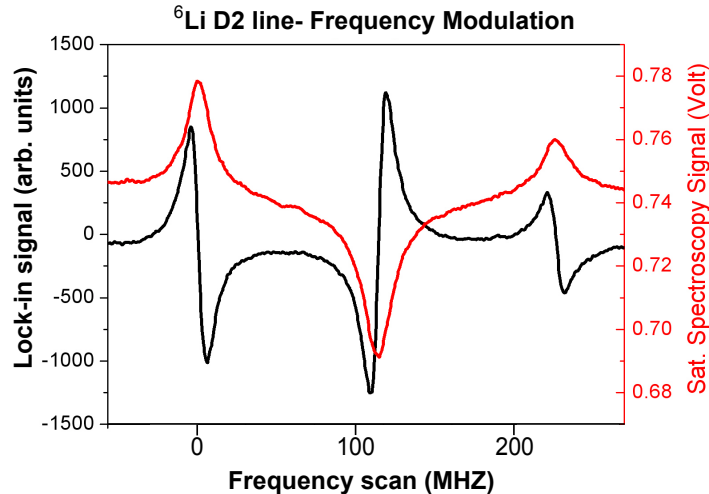


Figure 3.10: Absorption signal (red line) and error signal (black line) of the FM signal. The error signal is the derivative of the absorption signal. The zero of the x-axis is set at the frequency of $F=3/2$.

doesn't always happen at the desired point. This is due to Fabry-Perot effects, both in the windows and in the laser cavity itself, that introduce an offset in the derivative of the signal. This causes the zero-crossing not to exactly be at the transition frequency.

Modulation Transfer Spectroscopy

Modulation Transfer Spectroscopy (MTS) allows to achieve a better stabilization in the wavelength locking. MTS is performed using the same counter propagating beams as in FMS, but this time the pump beam passes through an Electro-Optical Modulator (EOM). EOMs are devices made out of a non-linear material which changes its refractive index in function of an applied external electric field. In this way an incoming electro-magnetic wave will experience a phase shift when passing through the EOM. If the external field has an oscillating behavior, the mod-

ulation of the electric field of the wave can be expressed as:

$$E = E_0 e^{i(\omega_i + M \sin \Omega t)} \quad (3.7)$$

where E_0 is the incoming field and E the out coming one, ω_i the frequency of the incoming laser, Ω the one of the oscillating applied electric field and M the amplitude of this modulation. Assuming $M \ll 1$, we find from eq.(3.7):

$$E \simeq E_0 e^{i\omega_i} (1 + iM \sin \Omega t) = E_0 (e^{i\omega_i} + \frac{M}{2} e^{i(\omega_i - \Omega)} + \frac{M}{2} e^{i(\omega_i + \Omega)}) \quad (3.8)$$

After passing through the EOM, two specular and weak sidebands appear in the out coming pump beam.

As shown in figure 3.11, the pump beam passes through the vapor cell where it interacts with the probe. When crossing inside the vapor cell, due to non-linearities

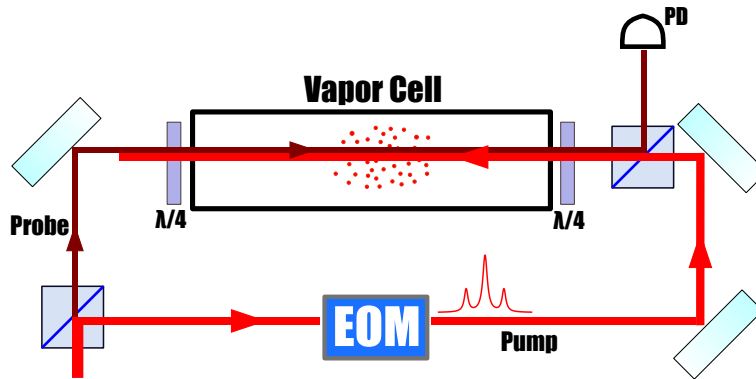


Figure 3.11: Optical scheme for the realization of MTS.

of the medium (the ${}^6\text{Li}$ vapor) and in particular due to effects of the third-order susceptibility χ^3 , two specular sidebands appear also in the probe beam at a difference in frequency corresponding to the modulation frequency. The generation of these sidebands is due to a four-wave mixing process.

After passing through the cell the probe is detected by a photo-detector. Here, the two sidebands beat on the detector and generate a signal composed by an in-phase component (absorption signal) and a quadrature one (dispersion signal). Both the absorption and the dispersion signal are odd functions of the detuning between the laser and the resonance frequency. Any linear composition of them can be used as an error signal in order to achieve laser locking (Fig 3.12).

Respect to FMS this technique has several advantages. First of all, the four-wave

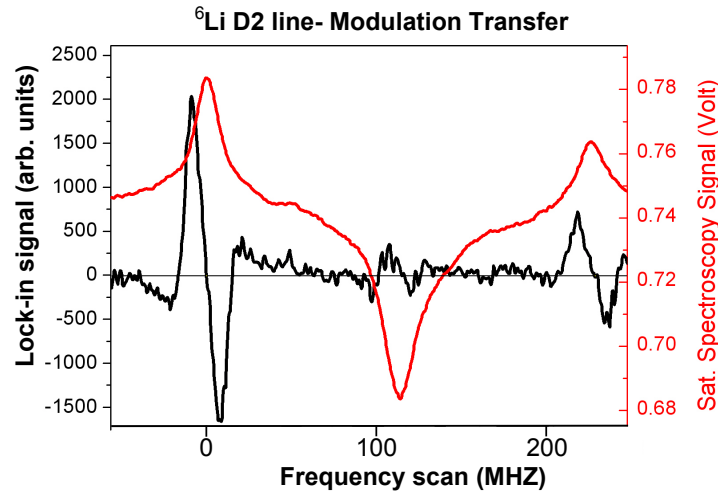


Figure 3.12: MTS absorption signal (red line) and MTS error signal (black). The error signal of the $F = 3/2 \rightarrow F' = 5/2$ is enhanced while the others, in particular the cross-over, are weakened. The zero of the x-axis has been arbitrarily set at the $F = 3/2 \rightarrow F' = 5/2$ transition.

mixing process happens only when the Doppler free resonance condition is satisfied and the absorption baseline becomes independent respect to any change in laser intensity or light polarization, leading to a zero background signal. Moreover the position of the zero-crossing keeps constant and doesn't slide away from the atomic transition. Among other advantages, the modulation is performed by an external object respect to the laser. In this way only the pump beam gets modulated, and not all the light coming out from the laser cavity, as it occurs in the FMS case. Since the error signal must be generated during the whole experimental sequence, if we use current modulation as in FMS, we can't avoid that all the light needed, not only the one used in the spectroscopic apparatus, will have some unwanted trace of modulation. Last but not least, the modulation frequency of the EOM can be very fast. In our case, we set this frequency at the value of 12.5 MHz. This makes the locking procedure more reliable, since the phase detecting software will experience less influence from noise sources, which are characterized by frequencies ranging from 10 to 100 KHz.

The error signal generated in our MTS scheme is shown in figure 3.12. Differently

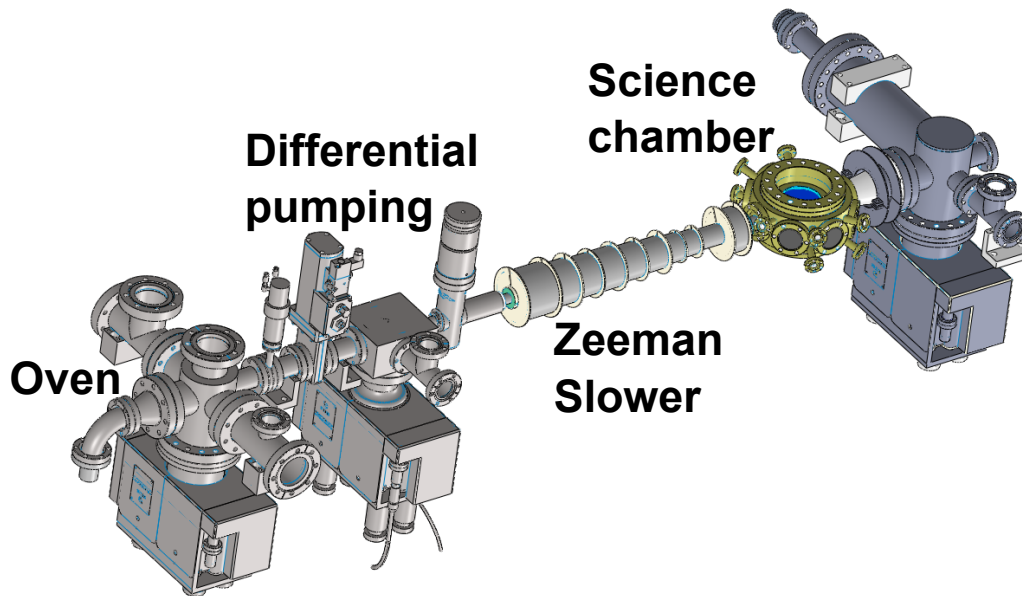


Figure 3.13: Overview of the experimental apparatus. The system starts on the left where the oven is placed. After this there are the differential pumping and the Zeeman slower. The system ends with the science chamber which has been colored in gold. The whole length is around 180cm.

from the FMS case, the cross-over signal is not present anymore, because the four-wave mixing process can happen only when the Doppler-free resonance condition is satisfied. Moreover, the four-wave mixing process is efficient only for closed transitions. This explains why in figure 3.12 there is one large signal at the D2 line position, thanks to the $F = 3/2 \rightarrow F' = 5/2$ transition, while the D1 signal is really weak.

3.4 Vacuum system

Here we are going to describe the heart of our experimental apparatus, the vacuum system, whose global overview is sketched in figure 3.13.

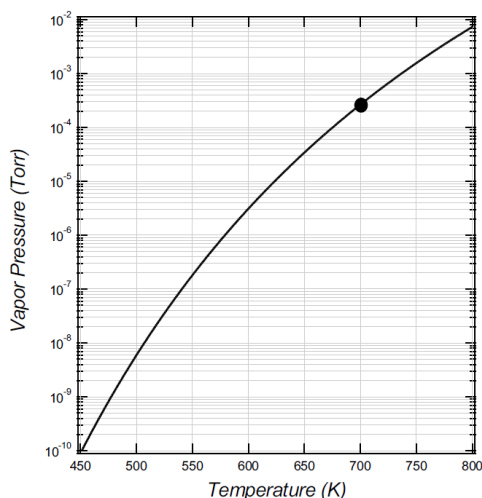


Figure 3.14: Lithium vapor pressure in function of absolute temperature. The black circle shows the typical temperature at which Li experiments are usually performed. Picture taken from [41].

3.4.1 The Oven

Since ${}^6\text{Li}$ is the less abundant of the two lithium isotopes (just 7% in nature), we decided to put in our oven an enriched sample of lithium with a 95% component of ${}^6\text{Li}$ (AMES Laboratory). The total amount of lithium is around 10 g. Differently from other alkalis, the vapor pressure of lithium is very low at room temperature (figure 3.14). For this reason, lithium is heated till 390 - 400°C in a bent cap wrapped in a heating ring. The cap acts as a lithium reservoir and, once heated up, allows the vapor to enter the apparatus by a hole on one of its side (figure 3.15). The position of this hole, called *nozzle*, is adjustable in order to achieve a better alignment of the out coming atomic beam. After the nozzle, the atoms pass through the *cold plate* which is a copper plate with an adjustable hole in its center, just like the one of the nozzle. Since it is cooled from outside with the help of a Peltier cell, this plate acts as a cold spot, where hot atoms which hit it will also stuck onto it. The purpose of the cold plate is too stop from the beginning those atoms with a wrong velocity direction for the cooling stage.

At the same height of the cold plate a titanium sublimation pump is located and next to it there is a valve to connect the oven to the pre-vacuum system. Below all of them an ion pump with a pumping speed of 75 L/s (STARCELL 75 L/s by Varian

Inc.) is placed. All these pumps are used for drastically reduce the pressure both in the oven and in the remaining part of the system. The bake out procedure will be explained later.

In the last part of the oven an pneumatic shutter (DS450VPS-P, Kurt Lesker) is found. This element can stop the atomic beam towards the Zeeman slower and the science chamber, putting a plate perpendicularly to their direction. In this way the thermal atomic beam won't interfere with the experiment in the science chamber once it is started. During the loading time, the shutter's plate will be placed alongside the direction of the atoms, allowing their passage.

The oven is closed by an ultra high vacuum gate valve (MDC, model 303012-03-11 DN40CF). This element, once closed, completely separates the oven from the remaining apparatus. In this way when the experiment is off the closed gate avoids undesired spreading of lithium in the rest of the apparatus, which can worsen the pressure in it. A drawing of some parts of the oven is reported in figure

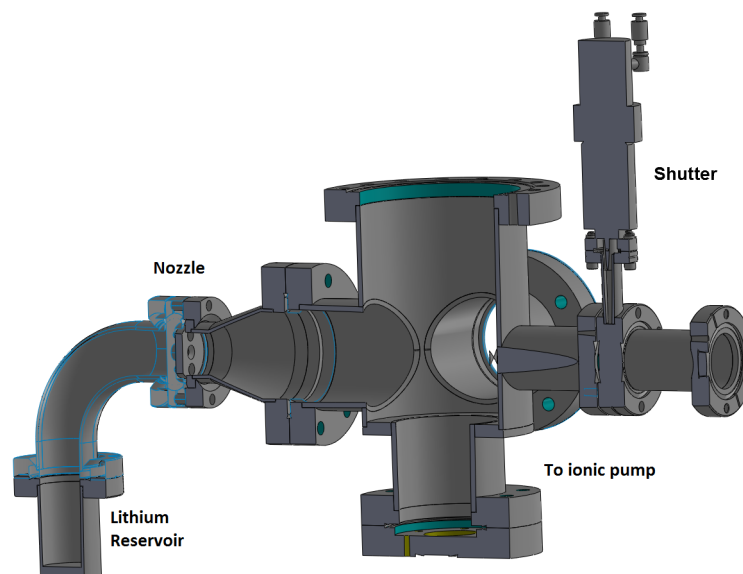


Figure 3.15: Drawing of the oven. The lithium reservoir and the nozzle are at the beginning of the system. After them there is the vacuum system. The gate valves and the cold plate are not shown.

3.4.2 Differential Pumping

After the gate valve there is the differential pumping stage, which is composed by two narrow tubes, oriented along the direction of the atomic beam. The two tubes are separated by 2.54 cm so that among them can operate both another pre-vacuum system and a second ion pump, smaller than the previous one and with a pumping speed of 55 L/s (STARCELL 55 L/s by Varian Inc.). The differential pumping is closed by a manual valve, which segregates this stage from the Zeeman slower.

The conductance of the differential pumping tubes is really small so that we can have a significant pressure difference between the oven and the science chamber. The goal of the differential pumping is preventing, thanks to the small conductance of the tubes, the pressure to equilibrate inside the system.

To estimate these difference, it is possible to treat the elements of our vacuum system more or less as the ones of an electric circuit [42]. The Ohmic-like law governing our system is the one relating the gas flux Q to the pressure difference ΔP among a channel of the system with conductance C and has the form:

$$Q = C\Delta P \quad (3.9)$$

The pumping elements are treated like elbows with conductance S , where S is their effective pumping speed, connecting the system to the ground, which is treated like a region with pressure equal to zero. For example, in the system represented in figure 3.16, we obtain the relation:

$$\frac{P_2}{P_1} = \frac{C}{C + S} \quad (3.10)$$

In our system, the differential pumping apparatus is schematically sketched in fig-

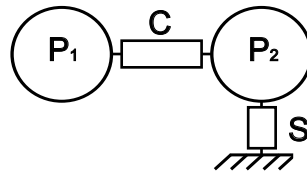


Figure 3.16: Two regions, with pressure P_1 and P_2 , are connected by an element of conductance C . The pump connects the P_2 region to the ground by an elbow of conductance S .

ure 3.17. At room temperature, the conductance of a tube of diameter d and length l can be approximated by the formula:

$$C = 12.1 \frac{d^3}{l} \quad (3.11)$$

The conductance in (3.11) has the dimensions of L/s if the diameter and the length are expressed in centimeters. The two tubes have a diameter of 4.6 mm and 7.7

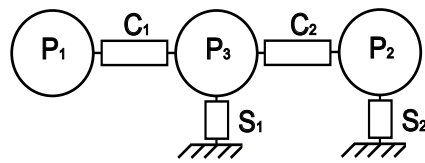


Figure 3.17: The intermediate ion pump among the tube is represented with the addition of another elbow to the ground.

mm and a length of 12.7 cm and 6.35 cm respectively. The ion pumps S_1 and S_2 have a pumping speed of 55 L/s and 75 L/s respectively. These values lead to a ratio among the pressures P_2 and P_1 of $3 \cdot 10^{-5}$. This means that if we manage to have a relatively high pressure of 10^{-7} mBar inside the oven, the pressure in the last part of the experiment will equilibrate at a value of approximately 10^{-12} mBar, which is an extremely good starting point for the preparation of a quantum degenerate gas. It has to be noted that without the small ion pump, among the narrow tubes, the pressure ratio would have been of the order of 10^{-3} : this would have required a significant reduction in the oven pressure. The drawing of the differential pumping components is reported in figure 3.18.

3.4.3 The Zeeman slower

The first laser cooling stage starts when the atoms enter the Zeeman slower. The Zeeman slower is a tube wrapped in coils, which creates a spatially inhomogeneous magnetic field. This magnetic field has to be calibrated in order to compensate for the changes in the Doppler shifts when atoms are cooled down by a counter propagating laser beam, entering into the system from a sapphire windows placed behind the science chamber. The spatial variation of this magnetic field allow us not to chirp the frequency of this laser beam.

As explained in paragraph 2.4.2, atoms can be trapped in a MOT only if they have

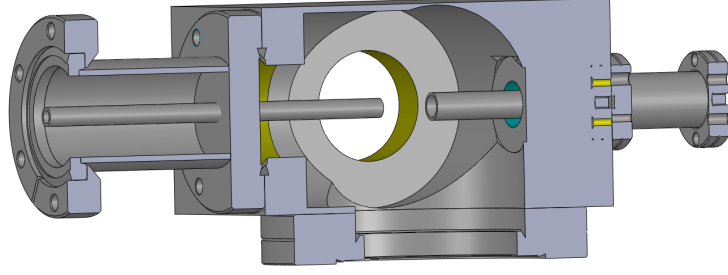


Figure 3.18: Drawing of the differential pumping stage and of the two narrow tubes. The ion pump is placed below their center.

a velocity lower than a certain one, called the capture velocity. The Zeeman slower is meant to affect the velocity distribution of an atomic vapor in order to increase the number of atoms with a velocity below the capture one. In our system, with an oven temperature around 400° , the mean velocity of the atoms coming out from the oven is around 1500 m/s, while the MOT is able to trap just atoms with a velocity slower than 60 m/s.

The shape of the required magnetic field can be found imposing the condition of maximum decelerating force acting on the atom. From eq.(2.21), we know that the force has a maximum when the effective detuning Δ_{eff} is zero, with:

$$\Delta_{\text{eff}} = \omega_L - \omega_0 + k_L v - \frac{\Delta E_{hs}(B)}{\hbar} \quad (3.12)$$

where $\Delta E_{hs}(B)$ is the hyperfine splitting of the cooling transition, dependent on the magnetic field.

For ${}^6\text{Li}$ atoms, as showed in figure 3.19, both the ground state's and the excited one's hyperfine levels enter the high field regime, also called Paschen-Back regime, at relatively small magnetic fields, i.e. for values larger than 100 Gauss for the ground state and larger then 3 Gauss for the excited one. From this we decided to set the cooling transition in the slower as the one from the $|m_j = 1/2\rangle$ in the ground state manifold at high fields to the $|m_j = 3/2\rangle$ in the excited one (figure 3.19), which can be driven by a σ^+ polarized beam. In the Paschen-Back regime, the hyperfine splitting among these states can be written as $\Delta E_{hs}(B) = \mu_B B$.

Putting it in the condition for zero effective detuning, we obtain the expression for

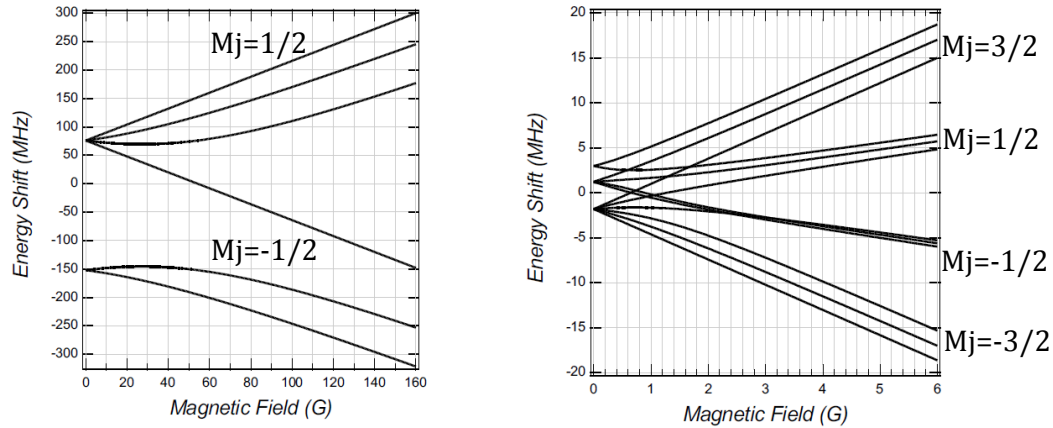


Figure 3.19: Dependence of the hyperfine energy levels of ${}^6\text{Li}$ in function of the magnetic field. Picture taken from [41].

the magnetic field:

$$B = \frac{\hbar}{\mu_B}(\Delta_0 + k_L v) \quad (3.13)$$

which, with the help of the kinematic formula at constant deceleration $v^2(z) = v_i^2 - 2az$, gives us an expression as the following:

$$B = \frac{\hbar}{\mu_B}(\Delta_0 + k_L \sqrt{v_i^2 - 2az}) \quad (3.14)$$

where v_i represents the maximum velocity which is slowed down by the slower.

For our slower, we have set $v_i = 830$ m/s and $\Delta_0 = -66.7\Gamma$, where Γ is the linewidth of the cooling transition. Moreover it has been assumed a constant acceleration a equal to one half of the maximum (eq. (2.15)), which corresponds in having the laser intensity equal to one. The calculated magnetic field is reported in figure 3.20.

This configuration of the magnetic field is called *spin flipping* Zeeman slower, since there is a region where the magnetic fields goes to zero. Here m_J stops being a good quantum number and it happens that some atoms exit the cooling cycle, which at high fields is a closed transition, falling into the state $|F = 1/2\rangle$ of the ground state. It is necessary to add another beam, called repumper, to bring back the atoms from the dark state $|F = 1/2\rangle$ into the cooling cycle.

A big advantage of this configuration is that the slowed atoms coming out from the Zeeman slower won't be in resonance with the counter propagating beam while they

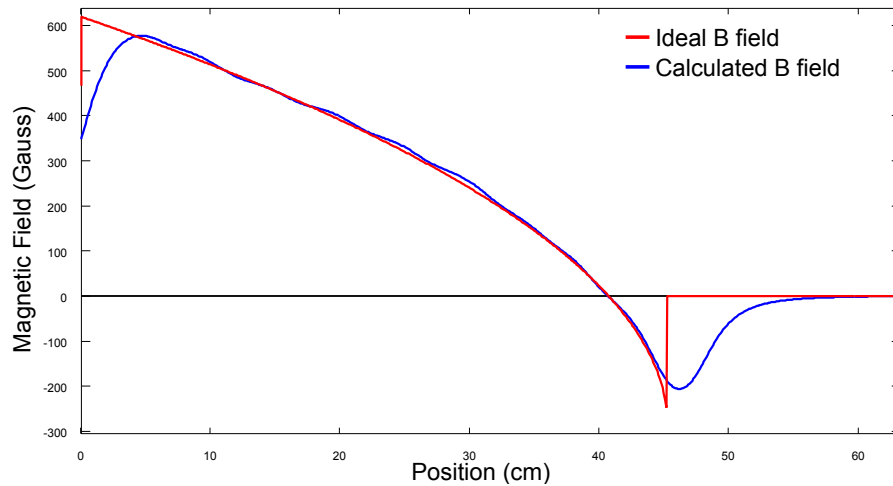


Figure 3.20: Comparison between the ideal magnetic field and the one calculated as superposition of the 9 coils of table 3.1.

travel towards the science chamber to load the MOT. Since this beam will have to be on for some time in order to efficiently load the MOT with an abundant amount of atoms, we'll need the already slowed down atoms to not interfere with the Zeeman laser beam, and this is actually the case. Moreover the required magnetic field doesn't need much electric power to be generated, reducing so the heating of the apparatus.

There were essentially other two possible solutions (figure 3.20) for our Zeeman slower:

- *Decreasing field configuration*: the detuning is such that the magnetic field is zero at the end of the slower. A relevant problem for this configuration is that atoms come out from the slower in resonance with the slowing beam. Because of their low velocity, it is possible that atoms are pushed back into the slower and do not enter into the chamber. A typical value for the detuning is about $\Delta = -10\Gamma$
- *Increasing field configuration*: the B field starts at zero and reaches a value around -800 Gauss at the end of the slower (the minus signs means that the current has a counter clock direction in the coils.) The disadvantage of this configuration is that we have an high field in the proximity of science chamber,

which can badly interfere with the field generated by the MOT. This large magnetic field also requires a relevant dissipated power to be generated. This may introduce undesired heating effect of the chamber.

In reason of this, we thought that the spin flipping slower better suits our needs. To generate such a magnetic field we have found the system of coils reported in the table 3.1 to be fine.

The theoretical magnetic field generated by the coils is reported in figure 3.20 and it has been used in a simulation in MATHEMATICA to check if the atoms were actually slowed down when put in such a field. As shown in figure 3.21, the velocities of the atoms are really affected by the combination of a counter propagating laser beam and the designed magnetic field and all the atoms having an initial velocity below 830 m/s exit the slower with a much smaller one. With these parameters the final velocity of the atoms is around 30 m/s.

The winding of all the coils for the slower was realized by an external company, which also cared about sticking them together with the help of a thermic glue, which can sustain temperatures up to 170°C.

Before enclosing the slower in the vacuum system, we measured the generated magnetic field with the help of a Hall probe, setting the different currents as the ones reported in table 3.1. The comparison among measurements and theoretical evaluation is reported in figure 3.22. The magnetic fields are slightly different, but the

Coils Number	Position (cm)	N° turns	N° windings	current (A)
1	0	68	28	2
2	7	48	22	2
3	12	48	19	2
4	17	48	17	2
5	22	48	14	2
6	27	48	11	2
7	32	38	7	2
8	36	33	4	2
9	44.5	35	22	-1.6

Table 3.1: Coils configuration to generate the required magnetic field for the Zeeman slower. The position expressed in the second column is intended from the beginning of the slower. The "N° turns" column and "N° windings" column show the number of loops in the longitudinal and radial direction respectively.

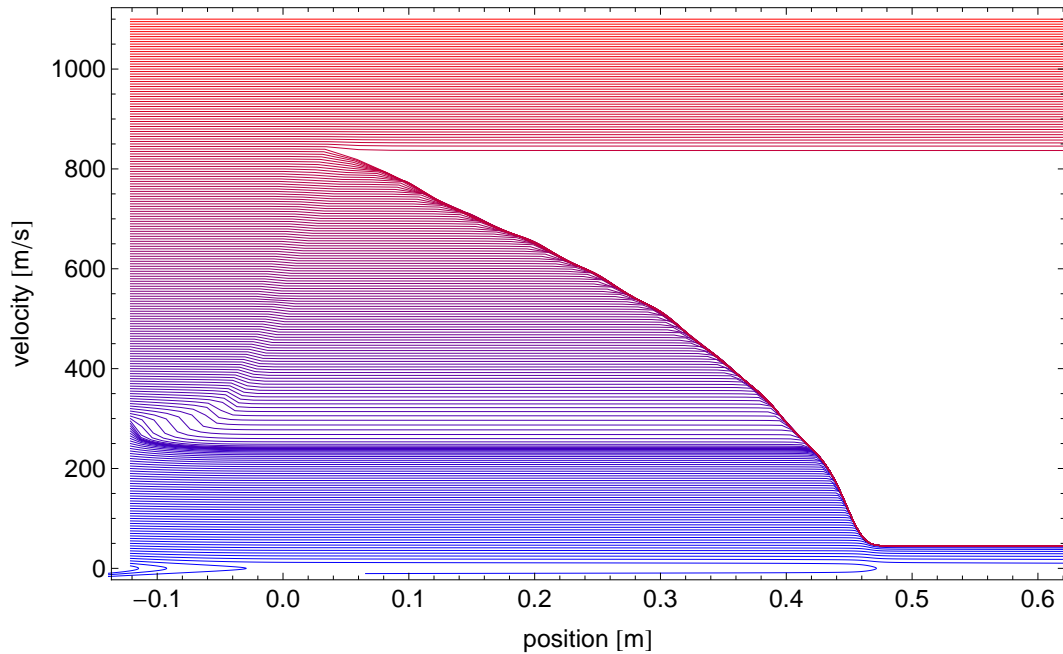


Figure 3.21: Spatial variation of the atoms' velocities inside the slower. The atoms with initial velocity below 830 m/s exit the slower with a significantly reduced velocity, while the ones which have a higher initial velocity are not affected by the Zeeman slower.

two slopes look very similar. We tried changing the current in the first 8 coils and found an optimal value with $I = 1.88\text{A}$. The resulting magnetic field is reported in figure 3.23, where it is still compared with the theoretical one. The agreement between the two now is really good. To check if the magnetic field is still effective in this configuration, we performed another simulation in MATLAB where we still found that the final velocity of the atoms is about 30 m/s.

3.4.4 Science Chamber

The atoms slowed down by the slower are collected by the MOT inside the science chamber, which is represented in figure 3.24. This chamber has been realized in order to provide us a very large optical access for the investigation of our experiments. The chamber, which is a custom project realized by KIMBALL PHYSICS, is made of stainless steel. It has 10 CF40 windows, lying in the apparatus plane, other 10 CF16 windows (MDC non-magnetic zero length fused silica viewport), disposed on as many steel branches tilted by 13° respect to the horizontal plane, and other

two large windows inside two CF100 flange on the top and the bottom of the cell.

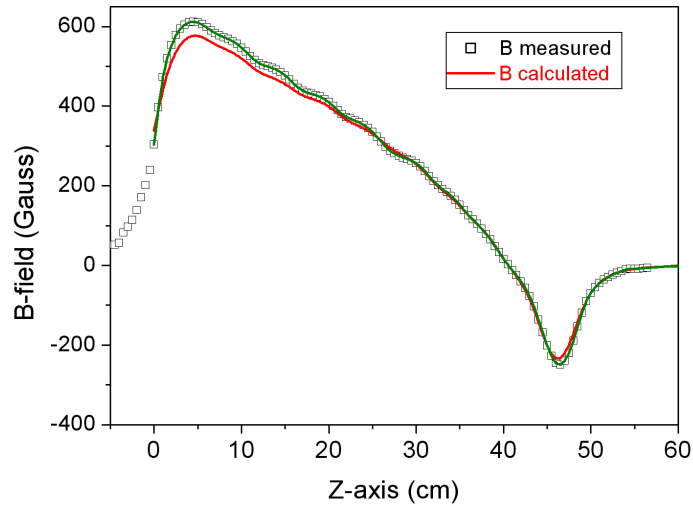


Figure 3.22: Comparison among the calculated magnetic field (white square), with a current of 2 A in the first 8 coils, and the theoretical one. The green line is the fit of the measured field.

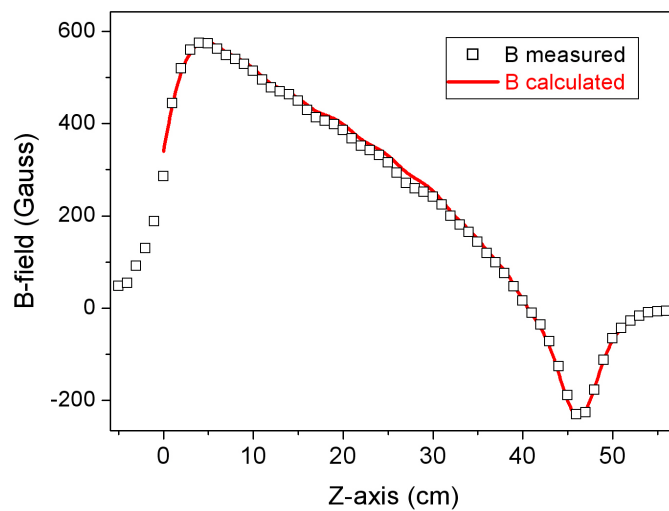


Figure 3.23: Comparison among the final configuration of the magnetic field and the theoretical one. The current in the first 8 coils has been set to 1.88 A.

Any of these windows has undergone an double-side anti-reflection (AR) coating procedure, realized by LASEROPTIK (Germany). This AR coating prevents the formation of undesired effects, for example spurious optical lattices, and will allow a better signal-to-noise ratio in the high resolution imaging procedure. The data about the reflection of the coated windows are reported in figure 3.25.

Optical access

The several windows will be used for different purposes (MOT beams, dipole traps, time of flight imaging,...) but among these the most challenging and interesting goal is the possibility to realize single-atom imaging of ultracold atoms in optical lattice. At the moment, single-atom detection has been proven only with bosonic samples [27, 43], which are generally more easy to handle respect to fermions. The first experimental papers where single atom imaging techniques were implemented immediately showed a lot of new and fascinating insights about the physics of many-body systems [44, 45] and so there is a lot of interest in realizing such techniques even for fermions.

High resolution imaging is usually realized placing a fluorescence microscope objective with both large numerical aperture (NA) and long working distance outside

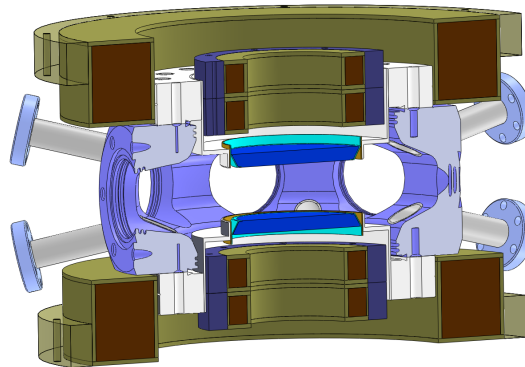


Figure 3.24: Section of the science chamber where all the relevant elements are shown. The big Feshbach coils lie on the edge of the cell while the other smaller coils are lodged inside the re-entrant view port. The view port ends with a thick and fused silica window (in bright blue in the picture) which will allow the high resolution imaging.

the chamber. Our re-entrant a-magnetic CF100 viewports (UKAEA) have been realized in order to allow the realization of this kind of objective. In particular these windows have been put on re-entrant supports so that the distance of their inner side from the center of the chamber would have been of just 12.7 mm. These fused silica windows are 6 mm thick and 60 mm large in diameter. One of the feature of this glass is having a wavefront error of less than 80 nm ($\lambda/8$ flatness at 670 nm). This is an important ingredient towards development of a high-resolution imaging. In figure 3.26 the first preliminary calculation of an objective, which may satisfy our requests, is drawn. This objective should collect on a CCD camera the fluorescent light coming from the atoms in the science chamber, with a resolution given by the formula:

$$R = 0.6 \frac{\lambda}{NA} \quad (3.15)$$

where R is the resolution and lambda the wavelength of the detected light, which is of 670 nm for lithium. Such an objective would grant us a resolution more or less equal to 670 nm, which for lithium is more than enough since these atoms are usually load in optical lattices with spacing larger than 1 μm to reduce their high tunneling rates due to their small mass [46].

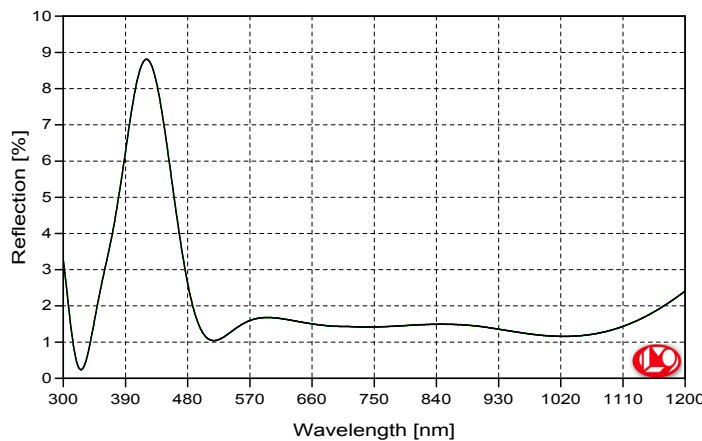


Figure 3.25: Double-side AR coating realized by LaserOptik for our windows. The coating has been extended also for different wavelengths respect to the one at 671 nm. The ones at 532 nm and 1064 nm will be useful for the creation of optical lattices. In absence of this coating the reflections of the windows would be of the order of 4%.

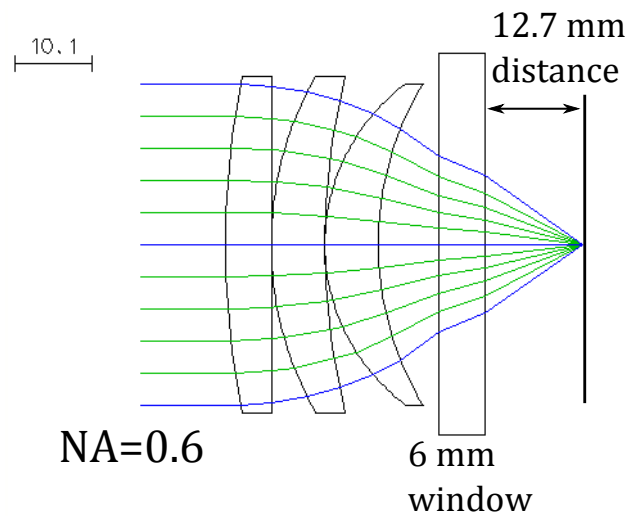


Figure 3.26: Sketch realized by us of a hypothetical fluorescence microscope for single atom detection. The objective has been corrected for spherical aberrations and has a $NA=0.6$ at 670 nm.

These microscope objectives can also be used not only to detect scattered light but also to create tailored optical potentials with sub micron resolution. This is possible thanks to the recent advances in the realization of Spatial Light Modulators (SLM) [47] which can be used in the realization of non conventional optical lattices like triangular or hexagonal ones, which are the key ingredient for the emergence of new and exotic phenomena in systems of great interest for the condensed matter community (frustrated systems, graphene,...).

Coils for magnetic fields

Magnetic fields are used also after the Zeeman slower stage inside the science chamber in order to complete the last steps of the experiment, both for the remaining passages of the cooling procedure and, later, for the control of the many-body system. We decided to create three different pairs of coils in order to satisfy our needs, which here and after will be named *Curvature Coils*, *Levitation Coils* and *Feshbach Coils*. Here we are going to describe only the theoretical calculation of these coils, since their realization required too much time and they couldn't be tested during the period of this thesis.

-
- Feshbach coils: this pair of coils is realized with a kapton insulated hollow wire with a cross section of 4.4 mm*4.4 mm. The coils have an inner radius of 78 mm and a layered structure with 7 windings in the horizontal direction and 8 in the vertical one, and will be placed on top of the science chamber. The main goal of these coils is to generate a magnetic field around 834 Gauss, because of the large Feshbach resonance ${}^6\text{Li}$ have at this value of the field. The coils are arranged in a way similar to the so called Helmotz configuration in order to reduce the gradient and the curvature of the magnetic field (figure 3.27). Having a small radial harmonic confinement is an important task for the realization of two dimensional system. In our case we can have at best a magnetic trap with radial harmonic frequency of about 10 Hz which is very low respect to typical values used in cold atoms experiments.
In this case hollow wire is required in order to perform water cooling of the coils from the inside and so reduce the heating due to the high dissipated power to generate such fields, which is more or less of 3.3 kW when working at 834 Gauss. Water cooling is performed connecting the wires to a high pressure chiller which in our case has to flux water into the coils with a pressure of 3 bar to prevent an increase in temperature of more than 25 Kelvin.
 - Curvature coils: this pair of coils is realized with a copper wire with a 1mm*3mm cross section. They have an inner radius of 28 mm, 7 windings in the horizontal direction and 4 in the axial one. Thanks to their reduced size and to the geometry of our chamber, they can be lodged inside the CF100 flange, really close to the viewport, in this way less current will be required to generate the desired magnetic fields, and so we can afford not to have water cooling for this pair. The purpose of these coils is to allow fast switches across the Feshbach resonance when studying the BEC-BCS crossover, since the large inductance of the Feshbach coils doesn't allow this. The side effect of using these coils is that, since they are quite far from being in a perfect Helmotz configuration, they introduce more magnetic gradient and curvature in the center of the trap. We have estimated for an hypothetical experiment an increase of the radial harmonic frequency to 13-14 Hz which is still a good configuration. The dissipated power in this situation can really be considered negligible (below 20 W).

The curvature coils will also be used for generating the magnetic field for the MOT stage. For this goal, the current in the two coils will circulate with opposite directions in order to create the field described in paragraph 2.4.2. The MOT field will have a gradient in the center of the trap of 30 Gauss per centimeter approximately. The required power for such a configuration is around 160 W, which won't dramatically heat up the science chamber.

- Levitation coils: this pair of coils is identical to the curvature one and will be placed in top of it inside the CF100 flange. We plan to use this coils with different currents circulating in them. In the most simple case just one of these coils will be on. This will introduce a large magnetic gradient along the vertical direction with a consequent force along it. This force may have the same or the opposite direction of the gravitational one and so we can think about increasing it, reducing it or even erasing it.

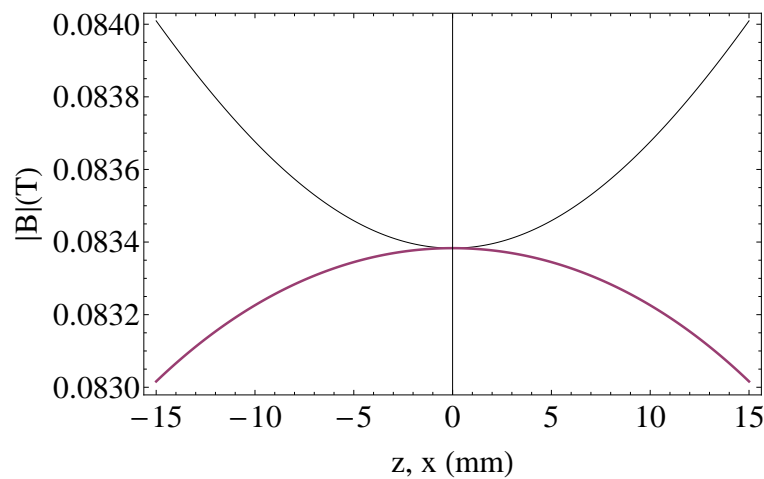


Figure 3.27: Theoretical behavior of the field generated by the Feshbach coils. The current has been set to 179.5 A to generate a field of 834 Gauss. The black curve is the field along the axial direction, the purple one along the radial one.

Actually we need another coil in our experimental system which is called *Compensation Coil*. This coil is placed after the science chamber and is concentric respect to the coils of the Zeeman slower. The purpose of this coil is to compensate for the non-vanishing Zeeman slower field in the center of the trap. Because of this, when turning the MOT field on, its minimum will not be placed in the center of the trap so the slowed down atoms cannot be trapped there. The shape of the coils has been

calculated in order to have a vanishing magnetic field in the center of the trap with a gradient smaller than 0.4 G/cm.

Position (cm)	N° turns	N° windings	current (A)
77	20	4	3.9

Table 3.2: Parameters of the compensation coil. The position is intended from the beginning of the slower.

3.4.5 Bake out procedure

To set the system to work, it is mandatory to achieve an extremely low pressure or ultra-high vacuum (UHV) in the science chamber. Typically, pressures below 10^{-10} mBar are required into the main cell.

Before assembling the vacuum system, any steel component was cleaned with acetone and an ultrasonic bath. Then they were put in an oven at a temperature around 350° for a period of 20 hours. This pre-vacuum procedure was needed to start degassing H_2 from the components' surfaces.

After the vacuum system was closed, the pumps were turned on. The pumps used in our experiment are a combination of titanium sublimation pumps, ion ones, and pre-vacuum system, generally composed by a scroll pump and a turbo pump. Any of these pumps is turned on at different stages of the vacuum procedure. The pre-vacuum system is the first one to be used and helps to reach pressures of the order of 10^{-8} mBar. The ion pump is turned on at the end of the baking procedure and allows to turn off the pre vacuum system, which is a source of mechanical noise, and to reach pressures of one or two orders of magnitude smaller. The titanium sublimation pump is the most peculiar stage. It is composed by three filaments which, when heated, spreads a titanium vapor all around. The titanium atoms glue part of the remaining particles inside the system to its wall. In this way the number of volatile particles is greatly reduced and so the pressure drops down, even below 10^{-12} mBar.

It is also required to heat the system up before activating the different pumps. The walls of our system before the baking are crowded with different atoms, in particular water, which compromise the quality of the vacuum in the cell. Heating the system up helps these atoms to detach from the walls so that they can be caught by the different pumps. Temperatures above $100^\circ C$ are required to detach water from

the walls. In our case, we succeeded in heating the system up to 200°C, as evenly as possible, for 5 days. In any part of the system, the ion pumps' gauges showed the low pressure signal, meaning that the pressure was below the lowest measurable one, which is actually 10^{-10} mBar. However in the next future a longer bake out procedure will be required, to decrease again the residual pressure in the system. It is common to perform the bake out for at least two weeks but because of the deadlines of this Master thesis, it couldn't be done in this period.

After the bake out we also noticed that when operating the oven at the proper temperature, around 400°C, the pressure in the oven raised till almost $5 \cdot 10^{-8}$ mBar, while the gauge in next to the science chamber was unaffected. This shows how the differential pumping works fine, preventing the oven to damage the vacuum in the other parts of the system.

Experimental Results

In this chapter we describe the realization of the MOT of lithium atoms. By optimizing the experimental parameters we obtained a cloud composed by 10^9 atoms at a temperature around $400 \mu\text{K}$ (figure 4.1).

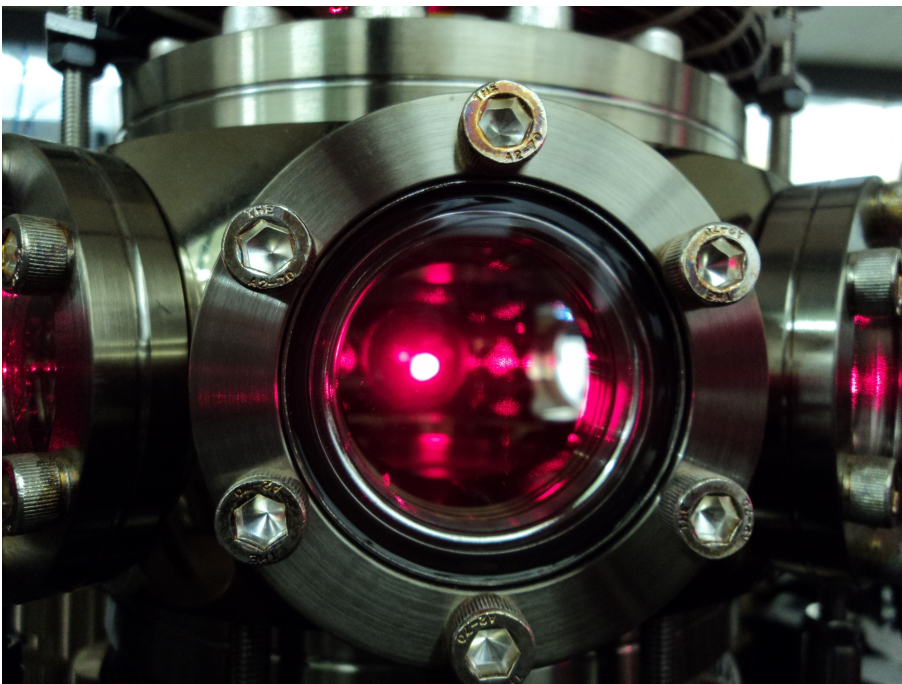


Figure 4.1: Photo of the cold atomic cloud trapped in the MOT.

4.1 Detection with a photodiode

For the optimization of the atom number trapped by the MOT, we look at the atoms through their emitted fluorescence signal, from which we can easily estimate the total atom number. The fluorescence signal from the MOT is collected onto a photodiode, placed just outside the science chamber (figure 4.2).

When shined by a laser beam, an atomic vapor will emit a fluorescence signal proportional to the absorbed light. The absorption depends on the scattering rate as already explained in chapter 2. We have to assume that the cloud is transparent to spontaneously emitted photons, so that the fluorescence signal will be directly proportional to the scattering rate and to the total atom number as well. Thanks to eq.(2.20) this can be written as:

$$V = AN\hbar\omega \frac{\Gamma}{2} \frac{I/I_s}{1 + I/I_s + (2\delta_0/\Gamma)^2} \quad (4.1)$$

where V is the intensity of the signal, N is the total atom number and A is the conversion factor of our detecting system. The constant A depends both on the response of the photodiode and on the fraction of solid angle covered by our imaging system. The final expression for the determination of the total atom number has the following form:

$$N = \frac{R}{V} \frac{\delta\Omega}{4\pi} \frac{2}{\hbar\omega\Gamma} \frac{1 + I/I_s + (2\delta_0/\Gamma)^2}{I/I_s} \quad (4.2)$$

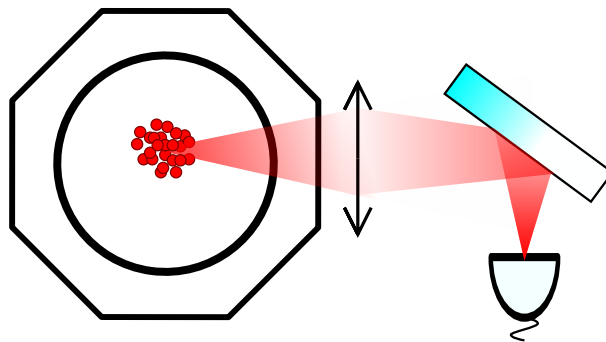


Figure 4.2: Sketch of the imaging system for the detection of the signal coming from the MOT. The light passing through one of the windows of the science chamber is focused with the help of a converging lens onto a photodiode.

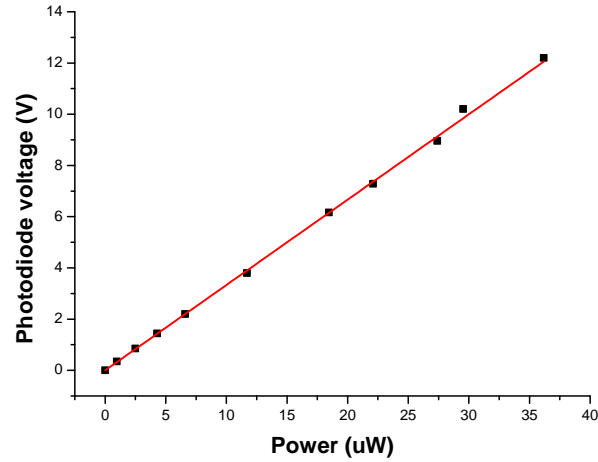


Figure 4.3: Dependence of the tension signal onto the photodiode in function of the incident power. The linear fit gives us the value of the response of the photodiode.

where R is the response of the photodiode and $\frac{\delta\Omega}{4\pi}$ is the fraction of solid angle.

4.1.1 Calibration of the photodiode

To perform our measurements we need to know the response of the photodiode. This is done independently shining laser beams with different and known intensities onto the photodiode and looking at the produced tension signal in an oscilloscope. The relation among the laser intensity and the tension response should follow the equation:

$$V = R \cdot I \quad (4.3)$$

where V is the tension signal, I the incident laser intensity and R the response of the photodiode which is the quantity we need to know.

The data of this calibration are reported in figure 4.3. We found a value of $R = 0.333 \pm 0.002 \text{ V}/\mu\text{W}$.

The portion of solid angle that our system is able to cover is evaluated considering the extension of the science chamber and one of its windows. To improve the signal to noise ratio, a large collimating lens has been placed outside a CF40 windows of the science chamber. All the emitted light passing through this window is focused onto the photodiode. With some geometrical calculation we estimated a solid angle

of $\frac{\delta\Omega}{4\pi} = (9 \pm 2) \cdot 10^{-3}$.

4.2 MOT loading

The MOT loading can be described by the the following differential equation:

$$\frac{dN}{dt} = L - \frac{N}{\tau} - \beta \int d^3r n^2(r) \quad (4.4)$$

where $\frac{dN}{dt}$ is the atoms' variation in time, L the loading rate and $n(r)$ the density distribution. The term τ is the lifetime of the trap in the low density regime, when the term proportional to $n^2(r)$ can be neglected. In this case the lifetime of the MOT is set by the pressure inside the science chamber. When colliding with the hot particles still inside the chamber, the cold atoms acquire too much energy and leave the trap. If instead the density is higher, collisions among the slowed atoms can no more be neglected. The term β in eq.(4.4) represents the two body losses coefficient. Light-assisted collisions are one of the reason for these losses. Two atoms in the ground state interact with a certain potential $V_{gg}(\vec{r})$. The absorption of a photon brings one atom in the excited state and makes the atoms interact with a different potential $V_{eg}(\vec{r})$. Generally, these excited level molecular potentials make the atoms accelerate towards the other. One the photon is spontaneously emitted, the two atoms may have acquired enough energy to leave the trap.

Assuming a gaussian distribution of the atoms inside the MOT, the eq.(4.4) can be written as:

$$\frac{dN}{dt} = L - \frac{N}{\tau} - \beta' N^2 \quad (4.5)$$

with:

$$\beta' = \frac{\beta}{(\pi/2)^{3/2} \sigma_z \sigma_r^2} \quad (4.6)$$

where σ_z and σ_r are the width of the gaussian distribution in the axial and radial direction respectively.

The presence of this term turns the decay of the MOT into a super-exponential one [48], described by the equation:

$$N(t) = N_0 \frac{e^{-t/\tau}/\tau}{1/\tau + N_0 \beta' (1 - e^{-t/\tau})} \quad (4.7)$$

The super-exponential behavior dominates at the beginning, while the regular one at following times, when part of the atoms has already been lost from the trap and the density dropped.

The behavior of the MOT loading will be affected mainly by the following parameters:

- Oven temperature
- Frequency detunings of the different laser beams
- Intensities of the different laser beams
- Gradient of the magnetic field

Since the MOT coils we designed weren't realized in time for this thesis, we used a pair of coils already existing in our lab. With this combination of coils we could realize a MOT field with a gradient of $2.4 \frac{\text{Gauss}}{\text{cm}}$ per circulating Ampere. The gradient is meant along the axial axis.

In the following sections we describe how we changed many experimental parameters to optimize the loading procedure.

Oven temperature

The temperature of the oven rules over the injected atomic vapor from the oven itself into the science chamber. The higher the temperature, the larger the loading rate L in eq.(4.4). A higher loading rate allows to increase the total atom number and to have a larger MOT. However, also the consumption of Li inside the oven would be enhanced and the lifetime of the metallic sample placed in it consequently reduced.

After the initial tries, when the temperature of the oven was pushed till the value of 490°C to raise the atomic flux and ease its detection, we decided to work at a value of 410°C . The configuration of our oven is very close to the one used in the Zwierlein's group at the MIT, which reported to work at a similar temperature.

The behavior of the MOT loading in function of the oven temperature is reported in figure 4.4. In figure 4.4 there is clearly a hint that shows a saturation behavior for the atom number into the MOT.

From the curves in figure 4.4 we extracted the loading rate at different oven temperatures. The results are shown in figure 4.5. The loading rate is increased when also,

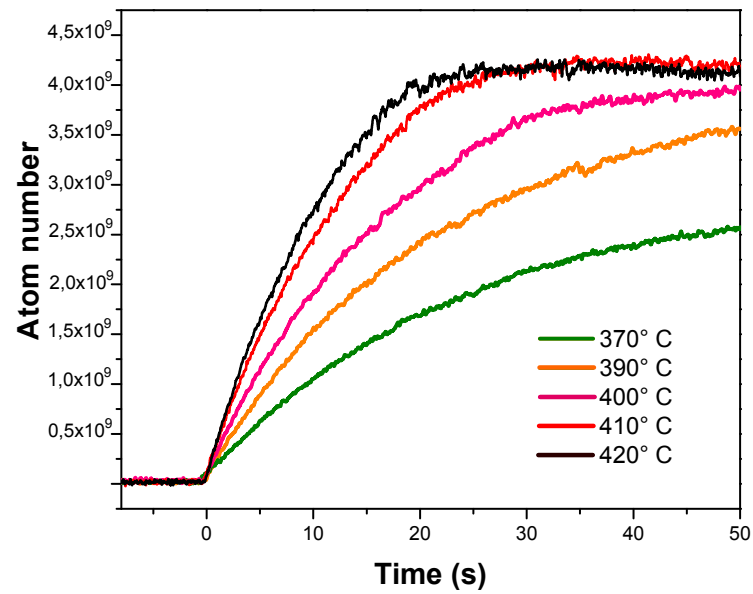


Figure 4.4: Atom number in the MOT at different temperatures of the oven.

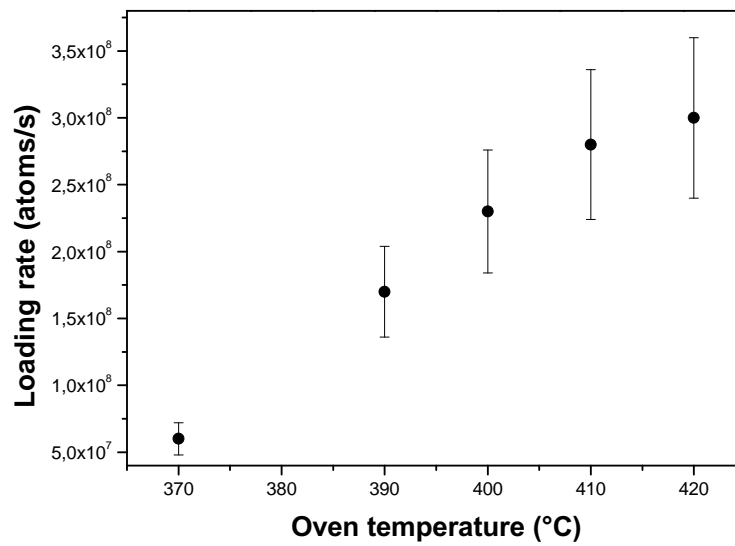


Figure 4.5: Loading rate at different oven temperatures.

but due to the finite dimension of our MOT beams, once reached a critical value for the atom density, two-body losses dominate the evolution of the system, preventing to increase the atom number. Increasing the temperature makes the loading faster, but doesn't increase the whole atom number. As already said, we decided to work at 410°C because the oven was meant to work at this temperature. We estimated that the sample in the oven has a lifetime of more than two years if working full time at this temperature.

Zeeman slower

The first stage we optimize was the cooling by the Zeeman slower. The Zeeman beam was made enter the vacuum system from the sapphire window placed behind the science chamber. Before entering the system, the beam was shaped to grant us the best slowing performance. The idea was to cover as much as possible the trajectory of the atoms inside the vacuum system. The beam had to be enlarged as much as possible by a telescope and then focused on the oven's nozzle with the help of a collimating lens. Because of the large distance among the sapphire window and the nozzle, no proper lens was founded. We so had to reduce the distance between the lenses of the telescope to have a non collimated beam, or in this case a diverging one. This was done before the loading of lithium in the oven to check with more accuracy the position of the focused beam.

The detuning of the Zeeman beam was set to a value $\delta_{\text{slower}} = -66.7\Gamma$, which was the one of the theoretical calculation. The value of the detuning of the MOT beams was set to $\delta_{\text{MOT}} = -6\Gamma$, for both the cooling and the repumper. The MOT magnetic gradient was set to a value of almost 20 Gauss/cm along the axial axis, according to our theoretical calculation in section 2.4.1.

Despite our measurements with the Hall probe, we had to change the current in all the coils of the Zeeman slower to increase the trapped atoms. Looking at the signal on the oscilloscope we found the values for the current in the coils reported in table 4.1. We believe that the difference among the theoretical values and the experimental one is due to a non perfect alignment of the Zeeman slower tube with the nozzle of the oven. The atoms feel a different magnetic field from the one evaluated in the middle of the tube. The currents reported in the table 4.1 were obtained moving slowly their value once the MOT loading saturated. The

Coil	current (A)
8 coils in series	2.34
spin flipping coil	-1.1
compensation coil	1.01

Table 4.1: Values of the current in the different coils of our Zeeman slower.

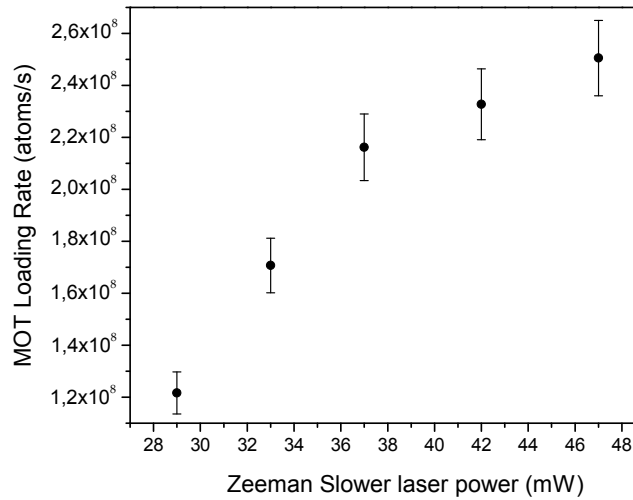


Figure 4.6: Loading rate for different intensities of the Zeeman beam. For high intensities the loading rate starts saturating.

calibration was done looking directly at the signal onto the oscilloscope, tuning the current in one of the coils till a maximum was reached and then moving to the others. The detection with the single photodiode is very convenient during this time of the characterization since it allows non destructive measurements of the MOT.

After this we optimized the power of the Zeeman slower beam. We found that the higher the intensity, the larger the atom number. The data are reported in figure 4.6 where the intensity of the Zeeman slower beam was controlled by changing the sound wave intensity in the relative AOM. We estimated a shot-to-shot fluctuation of 10%. This is generally due to fluctuations of the temperature of the oven or to different alignments of the mirror of our optical systems, which cannot be controlled so easily. Fluctuations in the laser power should be considered as well.

Looking at figure 4.6 it has to be noted that the loading rate increases linearly for

low intensities but then starts saturating. By increasing the power of the Zeeman beam we also increase the efficiency of the slowing stage till all the possible atoms are trapped. The maximum power achievable with the configuration of our laser setup is around 50 mW for both the cooling and the repumper.

As long as the detuning is concerned, the study of the loading rate in function of the Zeeman beam detuning couldn't be performed. This is due to the reduced efficiency of the Zeeman beam AOM. The AOM has a specific frequency response and the intensity of the out coming beam depends on the frequency we are using. The AOM is efficient just in a small band around its maximum of intensity, typically of the order of 10-20 MHz. To see a relevant change in the loading rate, the Zeeman beam detuning should have been changed by something around 100 MHz. When we tried to do so, the intensity of this beam was so low that the loading rate L was extremely weak and a comparison among the different detunings couldn't be realized.

4.3 Detection with a CCD camera

In this part we substitute the photodiode with a CCD camera (Stingray F-145B) in the imaging system. This CCD is a matrix of 1038x1388 pixels. The size of each pixels is of $6.4 \mu\text{m}$ per side. To image the atoms we implemented an optical system composed by two lenses, one with $f = 250 \text{ mm}$ and another one with $f = 45 \text{ mm}$. This system has an expected magnification $M = 0.18$. We experimentally measured the magnification of our optical setup by focusing a test target of known size on our CCD. The value we found is $M = 0.181 \pm 0.001$ and agrees with the expected one. With the CCD camera we can obtain directly the density distribution of the atomic cloud. The knowledge of this quantity allows us to extract the temperature of the cloud.

Calibration of the CCD

Similarly to what was done with the photodiode, also the CCD camera need to be calibrated. This is done by shining a laser beam of known intensity for a fixed period of time. The signal collected onto the CCD is then digitalized and analyzed by an imaging software, which can tell us the number of counts the CCD has performed while it was shined. Knowing the power of the incident laser beam and the energy of a single photon, we can obtain the ratio η among the number of counts revealed by the fitting program of the CCD and the number of photons shined onto the CCD

itself.

The number of photons can be evaluated with the formula:

$$N_{\text{ph}} = \frac{P t_{\text{exp}}}{\hbar\omega} \quad (4.8)$$

where P is the power of the laser beam, t_{exp} the period of exposure while the laser was on and $\hbar\omega$ the energy of a single photon.

In our calibration we set $P = 30 \mu\text{W}$ and $t_{\text{exp}} = 15 \mu\text{s}$. In this way the ratio η has the value:

$$\eta = \frac{N_{\text{counts}}}{N_{\text{ph}}} = 0.89 \frac{\text{counts}}{\text{photons}} \quad (4.9)$$

The quantity η is necessary when we try to estimate the amount of photon scattered by an atomic cloud by fluorescence, which is proportional to the atom number as previously explained.

Time-of-flight imaging

Time-of-flight (TOF) imaging is performed releasing the atoms from the trap. This is done by switching off the MOT beams and the quadrupole MOT field. To avoid undesired effects or spurious forces on the falling atoms, the Zeeman beam and the Zeeman slower's field are turned off too. After a short period of time, while the atoms expand, they're shined again by the MOT beams. The resulting fluorescence signal is collected by the CCD. The detuning of the MOT beams for the imaging has been set to $\delta = 0$ MHz, while their intensity doesn't change.

With TOF imaging we can always measure the atom number, by integrating the fluorescence signal on the array of photodiodes. The total number of counts by the CCD is first converted in number of photons through eq.(4.9) and then in atom number. The two quantities are related by the following equation:

$$\frac{N_{\text{photons}}}{t_{\text{exp}}} = N_{\text{atoms}} \frac{\delta\Omega}{4\pi} \frac{I/I_s}{1 + I/I_s + (2\delta/\Gamma)^2} \quad (4.10)$$

where t_{exp} is the time the probe beams were on.

Moreover the CCD allows to see the density distribution of the falling cloud. Its expansion is proportional to the velocity distribution of the atoms and so to their temperature. Assuming a gaussian distribution of the atoms in the MOT, the initial

atom number distribution can be approximated as:

$$N(x, 0) = \frac{N_0}{\sqrt{2\pi\sigma_0^2}} \exp\left(-\frac{x^2}{2\sigma_0^2}\right) \quad (4.11)$$

where σ_0 is the gaussian width of the atoms' distribution in the MOT, and N_0 the total atom number.

After a time of flight t since the MOT switching off, the initial gaussian distribution has evolved to a broader gaussian with width:

$$\sigma^2(t) = \sigma_0^2 + \langle v^2 \rangle t^2 \quad (4.12)$$

The term $\langle v^2 \rangle$ in eq.(4.12) is the mean quadratic velocity which has the following relation with the temperature:

$$\frac{1}{2}m\langle v^2 \rangle = \frac{1}{2}k_B T \quad (4.13)$$

In TOF we can obtain the value of $\sigma(t)$ by fitting the gaussian distribution revealed by the CCD after a time t of free expansion of the cloud.

We can write an expression for the temperature of the system simply as:

$$T = \frac{m}{k_B} \left(\frac{\sigma^2(t) - \sigma_0^2}{t^2} \right) \quad (4.14)$$

To obtain one picture of the expanding cloud three separate pictures are needed. The first is required to initialize the imaging system, it acts more or less as a cleaning of the CCD camera. The second one is the picture of the atoms which is obtained with the CCD open for a certain period of time. The last one is taken without the atoms and is needed to obtain the background signal of the imaging system. For obtaining this image the CCD is open for the same amount of time of the previous one and, after being digitalized by the imaging software, it is subtracted from the previous picture. The image realized by subtracting the last signal to the second one is our experimental data. This image is treated by the software as a two dimensional matrix: all the entries are the CCD pixel and the data stored are the counts revealed by the pixel itself. After the signal has been acquired, it is integrated once along the x direction and once along the y direction. The resulting figures obtained are

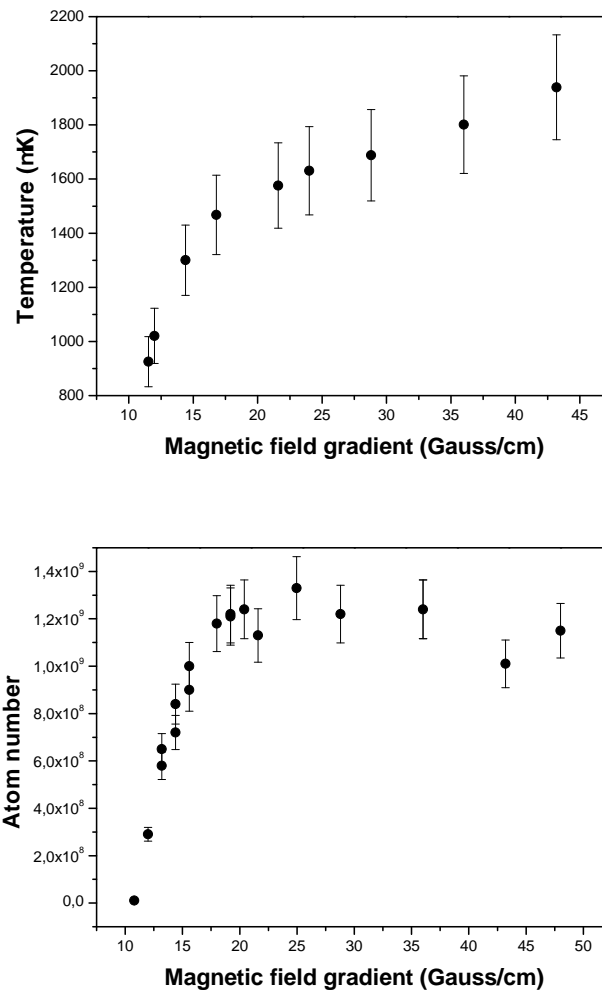


Figure 4.7: Atom number and temperature of the MOT after TOF imaging for different gradients of the MOT field.

two separate gaussians which can then be analytically fitted. The evaluation of the gaussian width and the knowledge of the time of flight gives us an estimate of the temperature.

MOT optimization

In this section we describe how we changed the parameters of our setup to characterize the MOT loading procedure. Large atom number and low temperature are both required for an efficient loading into the optical dipole trap. The parameters

we changed for this characterization are the gradient of the MOT magnetic field and the detuning of both the cooling and the repumper. At the beginning the detuning of the cooling and the repumper have been set to -4Γ , while the gradient to 25 Gauss/cm. The loading time has been set to 5 seconds.

We start looking at the temperature and atom number variation in function of the gradient of the MOT magnetic field. The data are reported in figure 4.7. Each point put in these pictures is the mean value of two measurements at the same conditions. The values for the temperature were obtained comparing the expansion of the cloud at two different times of flight. From eq.(4.12), the widths of the cloud at different times of flight are related by the equation:

$$\sigma_1^2 - \sigma_2^2 = \frac{k_B T}{m}(t_1^2 - t_2^2) \quad (4.15)$$

For this measurements, t_1 was set to 2 ms and t_2 to 0.5 ms. The direct measurement of σ_0 in the MOT is not reliable, since the density in the MOT is too high and the presence of magnetic fields modifies the scattering with the probe beams. We also controlled the time needed for the switch off of the MOT beams, the current in the coils and the magnetic field. The switch off of the MOT laser beams was monitored with a fast photodiode (bandwidth > 1 MHz). The timescale of this switch off is on the microseconds scale. We did the same for the current in the coils with the help of a transducer. The measured timescale was of the order of $300 \mu s$. The switch off of the magnetic field was instead measured with a Hall probe and we estimated a timescale around $500 \mu s$. We observe that there is an increase of temperature while increasing the gradient. From eq.(2.31) we know that the MOT elastic force increases for higher gradients. This also causes an increase of the atom density. Because of this two-body collisions are enhanced. In particular since the highest density region is the one in the center of the trap, where also the coldest atoms are located, losing atoms from the center means increasing the average temperature. Another effect that should be relevant is that the increase in density causes a raise of the scattering rates for the atoms, since they start absorbing also photons spontaneously emitted by other atoms in the cloud. This feature causes an increase of the temperature of the system. Basing on our measurements, we believe that the best compromise is achieved at a gradient of 24 Gauss/cm.

Similarly to what has been done with the gradient, we analyzed the variation of the

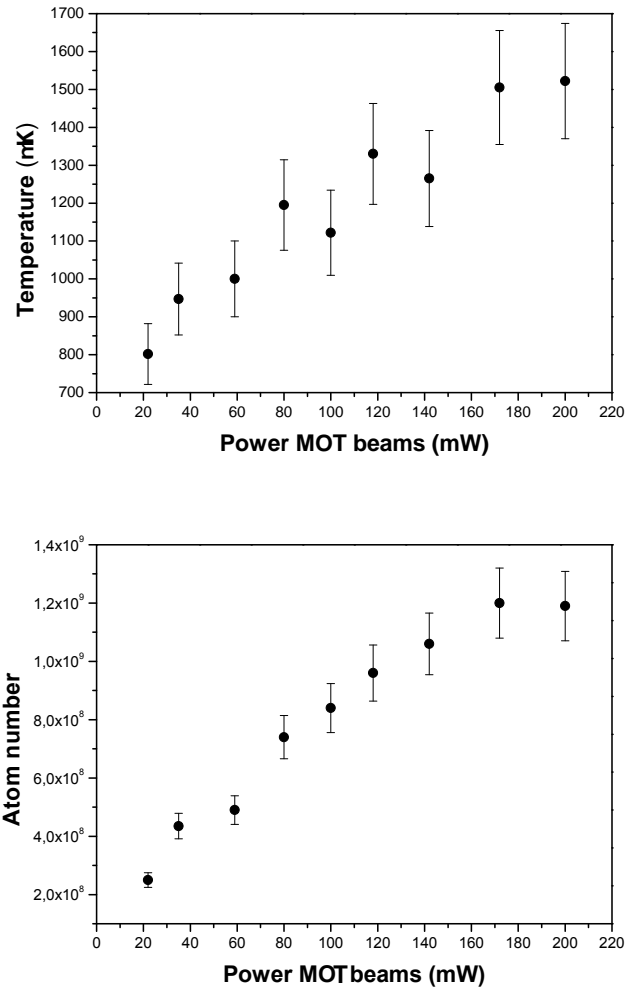


Figure 4.8: Atom number and temperature of the MOT after TOF imaging in function of the power of the MOT beams.

atom number and temperature in function of the power of the MOT beams. The results are reported in figure 4.8. We found that both the atom number and the temperature increase when the power of the beams increases. The increase in temperature can still be explained with a raise in the atoms' density inside the MOT. More intense MOT beams generate a stronger confining force, which from one side traps more atoms, but on the other increase the scattering rate in the system. For the following measurements the power of the beams has been set to the maximum available.

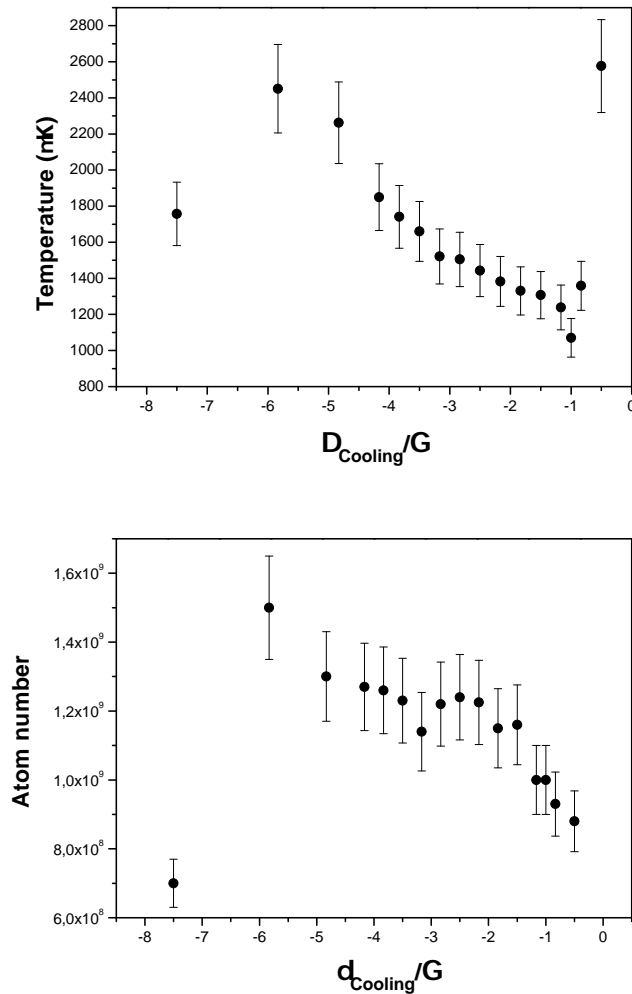


Figure 4.9: Atom number and temperature of the MOT after TOF imaging in function of the detuning of the cooling beam.

Another dependence we checked is the one in function of the detuning of the cooling beam. The data are reported in figure 4.9.

Again we found that when the atom number increases the temperature does the same. For the data in figure 4.9 this happens when the detuning becomes more negative. However, when approaching the resonance, the atom number keeps on decreasing while the temperature starts increasing after having achieved a minimum temperature around $1000 \mu\text{K}$ at $\delta = -\Gamma$. This behavior is the same as the one of equilibrium temperature in a molasses expressed by eq.(2.26). The difference

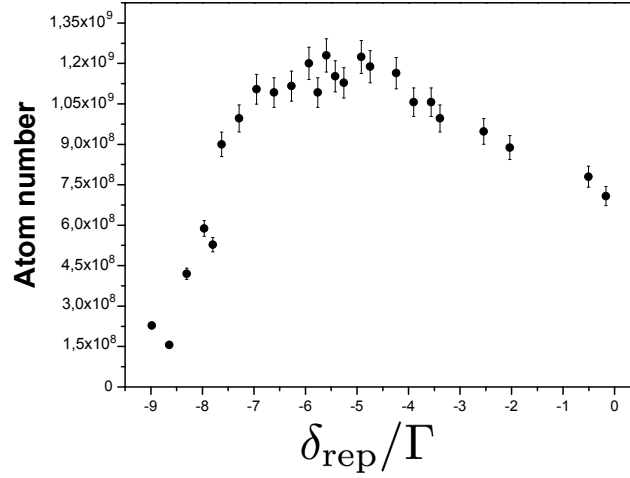


Figure 4.10: Atom number and temperature of the MOT after TOF imaging in function of the detuning of the repumper beam.

is that our minimum happens at $\delta = -\Gamma$ instead of $-\Gamma/2$. Additional comparison however cannot be performed because of the so large difference among the theory and experiment in the lithium case. There is at least one order of magnitude from the temperature predicted by the Doppler theory and the one observed by us.

We believe that the optimal condition is reached for a value of detuning for the cooling $\delta = -3\Gamma$.

The atom number was checked also in function of the repumper detuning. The data are shown in figure 4.10. For this case we didn't observed any significant variation of temperature by just changing the repumper detuning.

The best value for the repumper detuning is the one at -5Γ .

We repeated the temperature measurement for the MOT with TOF imaging for different times of flight, with the same experimental conditions of the previous optimization. The data are shown in figure 4.11 and we measure a temperature of 1.50 ± 0.11 mK. This value is a mean of the temperatures extracted from the different images in 4.11. As long as the atom number is concerned, we estimated a conservative error of about 30% on the absolute value of the atom number, due to uncertainties of some experimental parameters such as polarization and intensities of the beams, solid angle and real saturation intensity. In the measurement of figure 4.11, the atom number is $N = (1.0 \pm 0.3) \cdot 10^9$.

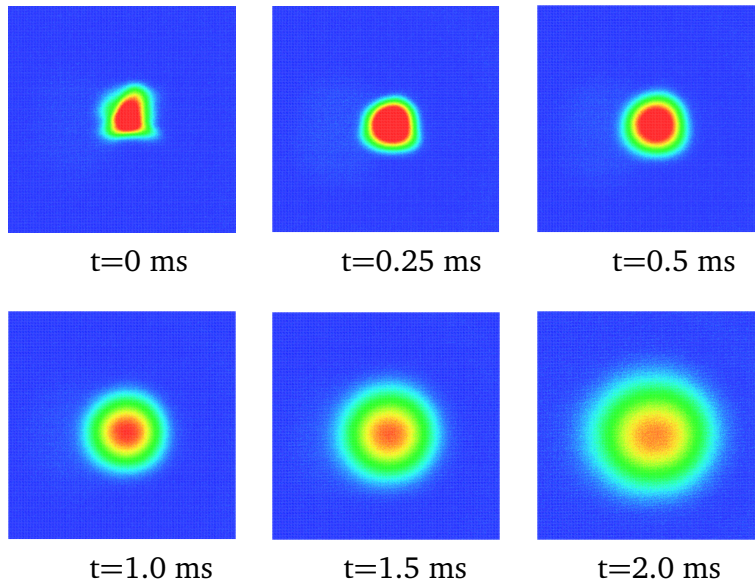


Figure 4.11: TOF imaging of the MOT for different times of flight. The temperature measured is of 1.50 ± 0.11 mK. The first image, the one with $t = 0$ ms in an *in-situ* image of the MOT. The time shown below each image represents the relative time of flight after which the image was taken.

The optimized experimental parameters are listed in the table 4.2.

We also studied the expansion of the cloud in free fall by looking at the evolution of its gaussian width in function of the time of flight. The data are reported in figure 4.12.

The value of temperature obtained from the data of figure 4.12 is $T = 1530 \pm 80 \mu\text{K}$. This value agrees with the one obtained by the direct TOF imaging, but this result is not so relevant since in the two cases we essentially use the same equation (eq.(4.12)) for the fitting. However, we could obtain a more precise value for the constant σ_0 of $1290 \pm 30 \mu\text{m}$.

$\partial B/\partial x$	δ_{cooling}	δ_{repumper}	N	T
24 Gauss/cm	-3Γ	-5Γ	10^9 atoms	1.5 mK

Table 4.2: Parameters of the MOT after the optimization.

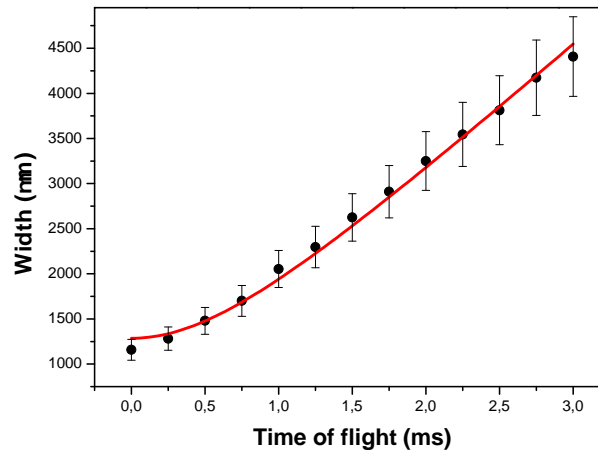


Figure 4.12: Evolution of the width of the atomic cloud in free expansion. The data were fitted with a function of the type: $y = \sqrt{\sigma_0^2 + \frac{k_B T}{m} x^2}$. We found a value for σ_0 of $1290 \pm 30 \mu\text{m}$.

MOT lifetime

Here we measured the lifetime of our MOT following the theoretical model described by eq.(4.7). We loaded the MOT with the Zeeman slower field off. Just the few atoms with velocity below the MOT capture one will be trapped. Such slow loading allows to obtain a cloud with very low density. We loaded the atoms for a period of 120 seconds and then closed the shutter and monitored the number of atoms still in the MOT versus the time. The results are reported in figure 4.13 and the fit has been realized both for the super-exponential decay and the regular one for low intensities. The super-exponential fit gave a lifetime $\tau = 240 \pm 18$ s. The regular exponential fit gave $\tau = 150 \pm 11$ s. The two results differ from each other but in any case we found a value of lifetime which is quite high and consistent with a pressure around 10^{-11} mBar inside the science chamber.

We also found a value for $\beta' = (8.4 \pm 2.5) \cdot 10^{-10} \frac{1}{\text{s} \cdot \text{atoms}}$. We estimated a width of 0.7 mm in all the three directions of the MOT distribution. We found a value of $\beta = (5.6 \pm 1.7) \cdot 10^{-13} \frac{\text{cm}^3}{\text{s} \cdot \text{atoms}}$. Our results are consistent with the values reported by other experiments [49, 50].

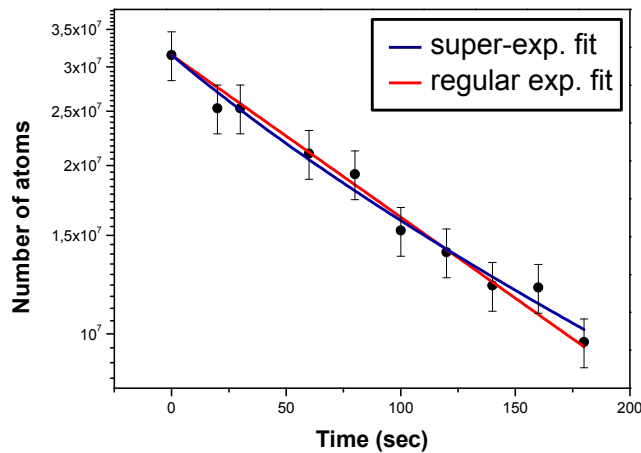


Figure 4.13: Decay of the MOT in function of time. The lifetime has been determined with both the super-exponential fit and the regular one. The values of the lifetime we have obtained are different from each other but consistent with the presence of an ultra-high vacuum region in the science chamber.

MOT temperature: *Release and recapture technique*

In this section we describe another technique, the so called release and recapture (R&R), for estimating the temperature of the MOT. This measurement has been done with the single photodiode and represents another way of obtaining the temperature of the system. The parameters of the experiment have been set to the one of the optimization of the previous paragraph.

For R&R measurement we set the loading time to 30 seconds, to make the MOT saturate. Then we turn off the MOT beams and magnetic field. In this way the atoms won't feel anymore the confining force and will escape from the trap, exactly what happens in TOF. After a short and controlled period of time both the MOT beams and the magnetic field are restored and the confining force as well. Hot clouds will broad faster than the cold ones, leaving less atoms in the trap region. With this technique we monitor the fraction of atoms still in the MOT in function of the time the MOT beams are off. We always start assuming a gaussian distribution of the atoms in the MOT, as the one in eq.(4.11). After a time t since the MOT switching off, the initial gaussian distribution has evolved to a broader gaussian

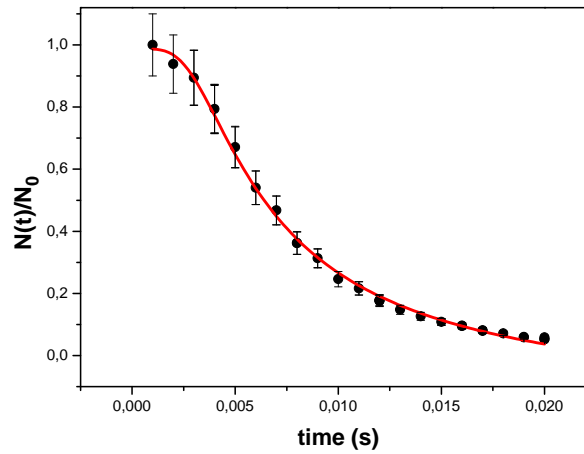


Figure 4.14: Data obtained from the release and recapture technique. For the fitting we used the following functions: $y = A \cdot \text{erf}(R_0/(\sqrt{2}\sigma(t))) + y_0$. The values of R_0 and σ_0 were fixed before the fitting to 5 mm and 1.3 mm respectively. These values agree with the real dimensions of both the laser beam and the initial MOT. The parameters A and y_0 are a limit of the theoretical model adopted in this description. It has to be noticed that eq.(4.17) doesn't give $\frac{N(t)}{N_0} = 1$ at $t = 0$. The parameters A and y_0 compensate for this limit of our model. Their fitted values are: $A = 1.189 \pm 0.009$ and $y_0 = -0.189 \pm 0.008$.

with width:

$$N(x, t) = \frac{N_0}{\sqrt{2\pi\sigma_t^2}} \exp\left(-\frac{x^2}{2\sigma_t^2}\right) \quad (4.16)$$

with σ_t expressed by eq.(4.12). When the MOT is turned on again, just the fraction of atoms inside the MOT capture radius R_0 will be trapped and detected again. The ratio of re-trapped atoms after time t can be expressed as:

$$\frac{N(t)}{N_0} = \text{erf}\left(\frac{R_0}{\sqrt{2}\sigma(t)}\right) \quad (4.17)$$

where $N(t)$ is the number of atoms still trapped and erf is the gaussian error function.

This method has several limitations. First we need several experimental shots to extract the temperature. Atom number fluctuates about 5-10% from one run to the

following one and this significantly affects the experimental data. Moreover, the theoretical model has some limits, in particular regarding the conditions for the atoms' re-trapping. However, it gives us another esteem of the temperature of the MOT. The data are reported in figure 4.14. The estimated temperature is $T = 850 \pm 110 \mu\text{K}$. This value of temperature doesn't agree very well with the one obtained from TOF. Because of the limitations of the R&R technique, we believe that TOF is by far the most accurate technique.

4.4 Compressed MOT stage

In this part we describe an additional cooling stage which is applied after the loading of the atoms. This is usually called compressed MOT (CMOT). The CMOT stage should allow to increase dimension and reduce the temperature of the initial MOT, making easier the loading of the atoms in the dipole trap for the evaporative cooling procedure.

This cooling scheme is based on some of the results obtained in our previous characterization of the MOT and it also follows the results reported in [51]. The first

	MOT loading (4.5 s)	Cooling stage I (199 ms)	Slower off (1 ms)	Cooling stage II (10 ms)	TOF (0-4 ms)	Imaging
Cool power	100%	45%		5%	0%	
Cool detuning	-3Γ	-2Γ				
Rep power	100%			5%	0%	
Rep detuning	-5Γ	-3Γ				
Gradient	24 G/cm			29 G/cm	0	
Slower beam	ON		OFF			
Slower field	ON		OFF			

Figure 4.15: Experimental sequence of the different phases to perform the additional cooling of the CMOT. The different sections report how much the parameters have been changed and for which amount of time. In the imaging section we have to restore the repumper 10 μs before the cooling to be able to detect the atoms. The second run that is in the imaging sequence is needed to obtain the image that the CCD will subtract from the previous one.

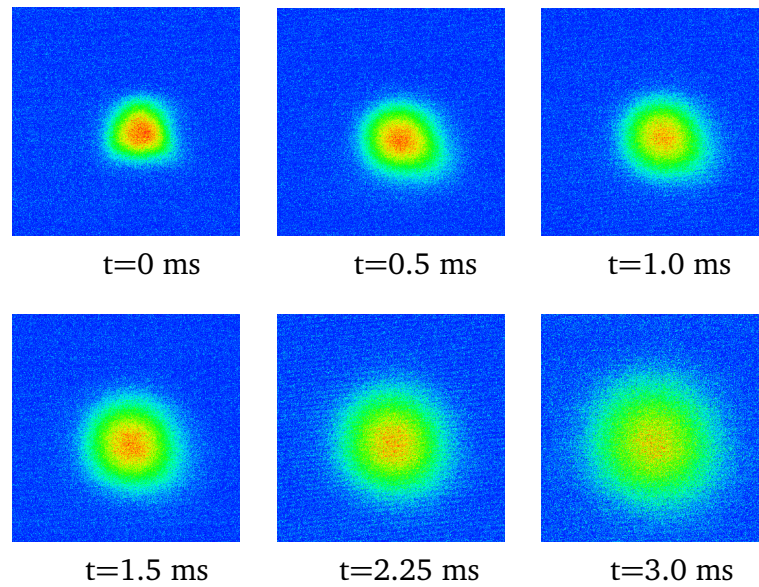


Figure 4.16: TOF images after the CMOT phase. Because of the reduced temperature, the atoms expand more slowly. This allows us to perform measurement for longer times of flight, since the atoms will still be inside the capture range of the probe beams, allowing their detection.

thing we do is reducing the intensity of the cooling beam (45% of the initial value) while still loading the MOT. At the same time we bring the detunings of both the beams closer to the atomic transition. As we have seen, this should start decreasing the temperature of the cloud (see data in 4.8 and 4.9). Then we stop the loading and dramatically reduce the power of both the cooling and the repumper while increasing the magnetic field gradient, to increase the density of the cloud. With the decrease of the repumper intensity, a large number of atoms falls in the $F = 1/2$ state. This is a so-called dark state, since atoms that are here don't scatter anymore photons from the cooling beams. The lack of absorption dramatically decreases the light-assisted collisions. These collisions are a limit when we try to increase the density of the cloud. When the density is high, the probability that some atoms will absorb the photons emitted by other atoms is increased. Atoms that interact in this way are coupled by an effective repulsive potential, which prevents an increase of the density. After this, we switch off everything and let the cloud expand to perform the usual TOF imaging. However, to detect the atoms that have fallen into the dark state, we need to restore the repumper at full power $10\mu\text{s}$ before the switch of the

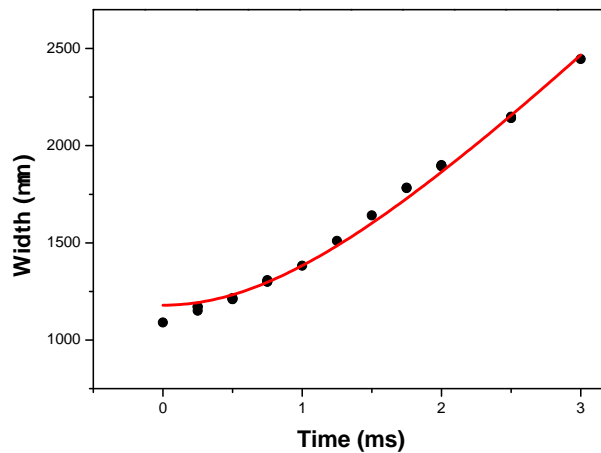


Figure 4.17: Evolution of the gaussian width after the CMOT phase. The evaluated value of the temperature is $T = 370 \pm 40 \mu\text{K}$.

cooling beam. The whole experimental sequence is reported in 4.15.

The temperature was extracted by fitting the evolution of the width of the distribution with the usual equation (4.12). Different images of the free-falling cloud are reported in figure 4.4 while the fitting is in figure 4.17. The value of temperature found was $T = 370 \pm 40 \mu\text{K}$.

During this additional cooling scheme it also happens that some atoms get lost. The images in the panel have an atom number around $N = (3.4 \pm 1.1) \cdot 10^8$, so less than half of the value of the regular MOT. This is due to the lower power of the repumper, which doesn't bring back all the atoms in the cooling cycle and some of them won't feel anymore the confining force and will leave the trap.

4.5 Phase-space density

The goal of laser cooling and evaporative cooling as well is too increase the phase-space density (PSD) of our atomic sample. The PSD can be written as:

$$PSD = n\lambda_{dB}^3 \quad (4.18)$$

where n is the density in real space and λ_{dB} the De-Broglie wavelength, which has the form:

$$\lambda_{dB} = \sqrt{\frac{2\pi\hbar^2}{mk_B T}} \quad (4.19)$$

In a quantum degenerate system the De Broglie wavelength is of the same order of magnitude of the inter particle distance, but at room temperature it is about 4/5 order of magnitude smaller. The only parameter that can be changed to increase this quantity is the temperature and this is actually the purpose of laser cooling.

If we consider the case of our experiment, the lithium is initially at a temperature of 700 K. Referring to figure 3.14, the lithium vapor pressure p in our oven is about $5 \cdot 10^{-3}$ mBar, which means that the number density is $n = \frac{p}{k_B T} \simeq 4 \cdot 10^{16}$ atoms/m³, while the De Broglie is approximately $\lambda_{dB} \simeq 10^{-11}$ m. With these conditions, the PSD is of the order of 10^{-15} , so very far below the required value for quantum degeneracy.

In the MOT we realized, the PSD is instead much higher respect to the previous case. The number density in the MOT is evaluated by the formula $n = \frac{N}{\sigma_r^2 \sigma_z}$ where N is the total atom number in the MOT and the σ_i s are the gaussian width of the MOT in the different directions. The value of the number density is around 10^{17} atoms/m³, but the drop in temperature makes the De Broglie wavelength increase a lot. For a MOT at $T = 1.5$ mK, we have $\lambda_{dB} = 10^{-8}$ m and consequently an increased PSD value of 10^{-6} .

With our last stage, the CMOT one, the further decrease in temperature increases again both the De Broglie wavelength and the PSD. In our coldest cloud at $T = 370 \mu$ K and with $N = 4 \cdot 10^8$, the PSD is around 10^{-5} .

This is still very far from quantum degeneracy, but our value of PSD is very close to experimental limit achievable in a MOT [52].

Conclusions and Outlook

During the period of this Thesis we succeeded in producing a cold sample of ${}^6\text{Li}$ atoms trapped in a magneto-optical trap (MOT). By a systematic optimization of the experimental parameters, we could trap and cool about 10^9 atoms to temperatures of the order of hundreds of micro Kelvin thanks to standard laser cooling techniques. This corresponds to a phase space density (PSD) of about 10^{-5} .

To obtain this cold sample, we have realized a new generation experimental apparatus. The whole vacuum and laser system have been assembled from the beginning during the period of work in the lab.

The results presented in this Thesis are a very good starting point to proceed with further cooling stages in a pure optical trap to enter the quantum degenerate regime.

The atoms will be then transferred in two-dimensional optical potentials. Here we plan to implement Fermi-Hubbard Hamiltonians, which can be written as:

$$H = -t \sum_{\langle i,j \rangle, \sigma} (c_{i,\sigma}^\dagger c_{j,\sigma} + h.c.) + U \sum_{i=1}^N n_{i\uparrow} n_{i\downarrow}$$

They are realized superimposing impurity-free optical lattices onto the 2D layers, controlling both the hopping energy t by optical lattice depth and the on-site interaction U by Feshbach resonances (see figure 5.1).

These Hamiltonians are proposed as minimal models for explaining the behavior of electrons in high-Tc superconductivity. The phase diagram of these models is con-

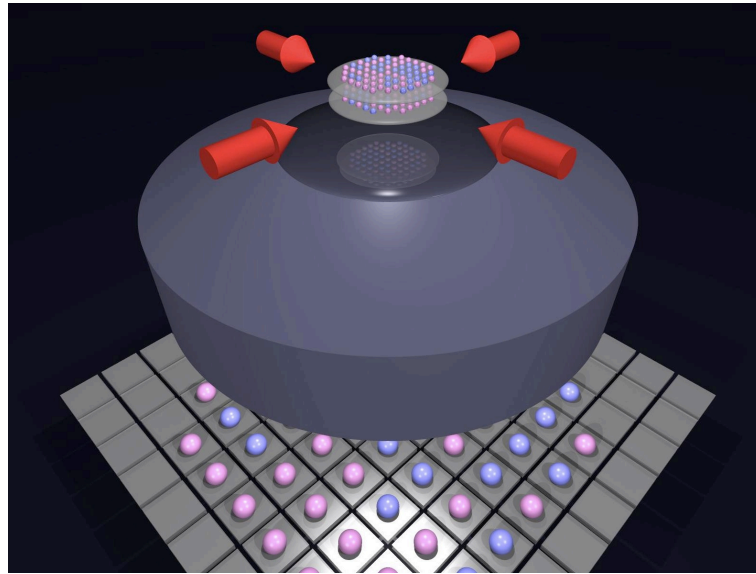


Figure 5.1: Pictorial view of ultracold layered fermions trapped in a square optical lattice. A microscope objective will be placed close to the atomic layers to extract with high resolution the correlation functions of the system. This setup is an experimental implementation of Fermi-Hubbard Hamiltonians.

sidered the Holy Grail in the theory of strongly correlated systems. There are two limits that are well established. At half filling (one particle per lattice site) the model describes a Mott insulator phase, while below the Neel temperature it describes an anti-ferromagnet. Far from the half filling (doped regime) the nature of the ground state is largely under debate. One possibility is that this model support the d-wave superconducting phase at high- T_c . At the moment there is neither analytical nor numerical results that can support conclusively this hypothesis.

For these reasons, we believe that the implementation of such Hamiltonians in our system will provide important indications on the ground states of these Hamiltonians, shining new light on the physics of strongly correlated 2D fermions.

Ringraziamenti

Un grazie speciale lo voglio riservare per i membri del gruppo Litio: Giacomo, Alessia ed il muchacho Jorge Amin. In questo anno avete pazientemente (piú o meno) risposto alle mie domande e risolto i miei mille dubbi, oltre ad avermi introdotto con entusiasmo alla fisica sperimentale. Grazie ancora.

Un grazie speciale va ad i professori Inguscio e Benedek, chi per avermi accolto a braccia aperte e chi per aver messo una buona parola sulla fiducia.

Un grazie anche al dottor Montalenti per aver accettato di darmi una mano per il sostenimento della tesi.

Desidero ringraziare anche tutti gli altri membri del gruppo di Gas Quantistici che hanno reso il trapianto a Firenze molto piú digeribile.

Infine ringrazio la mia famiglia che mi ha costantemente supportato ed aiutato in questo anno lontano da casa. Questo lavoro é dedicato a voi.

Bibliography

- [1] Feynman R.P. Simulating physics with computers. *International Journal of Theoretical Physics*, 21(6/7):467–488, 1982.
- [2] Trabesinger A. et al. Nature Physics insight: Quantum Simulation. *Nature Physics*, 8(4):262–299, 2012.
- [3] Bloch I., Dalibard J., Zwirger W. Many-body physics with ultracold atoms. *Review of Modern Physics*, 80(4):885–964, 2008.
- [4] Petrov D.S., Holzmann M., Shlyapnikov G.V. Bose-Einstein condensation in quasi-2D trapped gases. *Physical Review Letters*, 84(12):2551–2555, 2000.
- [5] Burger S., Cataliotti F.S., Fort C., Maddaloni P., Minardi F., Inguscio M. Quasi-2d bose-einstein condensation in an optical lattice. *Europhysics Letters*, 57(1):1–6, 2005.
- [6] Inouye S. et al. Observation of Feshbach resonances in a Bose-Einstein condensate. *Nature*, 392(6672):151–154, 1998.
- [7] Chin C., Grimm R., Julienne P., Tiesinga E. Feshbach resonances in ultracold gases. *Reviews of Modern Physics*, 82(2):1225–1286, 2010.
- [8] Struck J. et al. Quantum simulation of frustrated classical magnetism in triangular optical lattices. *Science*, 333(6045), 2011.
- [9] Jonathan S. et al. Quantum simulation of antiferromagnetic spin chains in an optical lattice. *Nature*, 472:307–312, 2011.
- [10] Tarruel L. et al. Creating, moving and merging Dirac points with a Fermi gas in a tunable honeycomb lattice. *Nature*, 483:302–305, 2012.

- [11] Greiner M., Mandel O., Esslinger T., Hansch T.W., Bloch I. Quantum phase transition from a superfluid to a Mott insulator in a gas of ultracold atoms. *Nature*, 415(6867):39–44, 2002.
- [12] Billy J. et al. Direct observation of Anderson localization of matter waves in a controlled disorder. *Nature*, 453:891–894, 2008.
- [13] Roati G. et al. Anderson localization of a non interacting Bose-Einstein condensate. *Nature*, 453:895–898, 2008.
- [14] Baumann K., Guerlin C., Brennecke F., Esslinger T. Dicke quantum phase transition with a superfluid gas in an optical cavity. *Nature*, 464:1301–1306, 2010.
- [15] Bednorz J.G., Muller K.A. Possible High-Tc superconductivity in a Ba-La-Cu-O system. *Zeitschrift fur Physik B: Condensed Matter*, 64(2):189–193, 1986.
- [16] Hadzibabic Z. et al. Berezinskii-Kosterlitz-Thouless crossover in a trapped atomic gas. *Nature*, 441:1118–1121, 2006.
- [17] Feld M. et al. Observation of a pairing pseudogap in a two-dimensional Fermi gas. *Nature*, 480:75–78, 2012.
- [18] Sommer A. et al. Evolution of fermion pairing from three to two dimensions. *Physical Review Letters*, 108(4):045302, 2012.
- [19] Salomon C. Inguscio M., Ketterle W., editor. *Proceedings of the International School of Physics "Enrico Fermi" - Course CLXIV "Ultra-Cold Fermi Gases"*, 2007.
- [20] Bourdel T. et al. Experimental study of the BEC-BCS crossover region in lithium 6. *Physical Review Letters*, 93(5):050401, 2004.
- [21] Tinkham M. *Introduction to Superconductivity*. Dover, 1996.
- [22] Leggett A.J. *Quantum Liquids: Bose Condensation and Cooper Pairing in Condensed-Matter Systems*. Oxford Graduate Texts, 2006.
- [23] Chen Q. et al. BCS-BEC crossover: From high temperature superconductors to ultracold superfluids. *Physics Reports*, 412:1–88, 2005.
- [24] Anderson P.W. *The Theory of Superconductivity in the High-Tc Cuprate superconductors*. Princeton University Press, 1997.

- [25] Lye J.E., Fallani L., Modugno M., Wiersma D.S., Fort C., Inguscio M. Bose-Einstein condensate in a random potential. *Physical Review Letters*, 95(7):070401, 2005.
- [26] Dubi Y., Meir Y., Avishai Y. Nature of the superconductor-insulator transition in disordered superconductors. *Nature*, 449:876–880, 2007.
- [27] Bakr W.S. et al. A quantum gas microscope for detecting single atoms in a Hubbard-regime optical lattice. *Nature*, 462:74–77, 2009.
- [28] Hansch T.W., Schlow A.L. Cooling of gases by laser radiation. *Optics Communications*, 13(1):68–69, 1975.
- [29] Bose S.N. Plancks gesetz und lichtquantenhypothese. *Zeitschrift fur Physik*, 26:178–181, 1924.
- [30] Anderson M.H. et al. Observation of Bose-Einstein Condensation in a dilute atomic vapour. *Science*, 269(5221):198–201, 1995.
- [31] Hess H.F. Evaporative cooling of magnetically trapped and compressed spin-polarized hydrogen. *Physical Review B*, 34(5):3476–3479, 1986.
- [32] DeMarco B., Jin D.S. Onset of Fermi degeneracy in a trapped atomic gas. *Science*, 285(5434):1703–1706, 1999.
- [33] Metcalf H.J., van der Straten P. *Laser Cooling and Trapping*. Springer, 1999.
- [34] Raab E.L., Prentiss M., Cable A., Chu S., Pritchard D.E. Trapping of neutral sodium atoms with radiation pressure. *Physical Review Letters*, 59(23):2631–2634, 1987.
- [35] Lett P.D. et al. Observation of atoms laser cooled below the doppler limit. *Physical Review Letters*, 61(2):169–172, 1988.
- [36] Duarte P.M. et al. All-optical production of a lithium quantum gas using narrow-line laser cooling. *Physical Review A*, 84(6):061406(R), 2011.
- [37] G. Roati et al. K-39 Bose-Einstein condensate with tunable interactions. *Physical Review Letters*, 99(1):010403, 2007.

- [38] Petrov D.S., Salomon C., Shlyapnikov G.V. Weakly bound dimers of fermionic atoms. *Physical Review Letters*, 93(9):090404, 2004.
- [39] Müller T. *Microscopic probing and manipulation of ultracold fermions*. PhD thesis, ETH Zurich, 2011.
- [40] Stan C.A. *Experiments with interacting Bose and Fermi gases*. PhD thesis, MIT Boston, 2005.
- [41] Gehm M.E. *Preparation of an optically-trapped Degenerate Fermi Gas of ^6Li : Finding the route to degeneracy*. PhD thesis, Duke University, 2003.
- [42] Salez T. *Towards quantum degenerate atomic Fermi mixtures*. PhD thesis, ENS-LKB Paris, 2011.
- [43] Sherson J.F. et al. Single-Atom resolved fluorescence imaging of an atomic mott insulator. *Nature*, 467:68–72, 2010.
- [44] Bakr W.S. et al. Orbital excitation blockade and algorithmic cooling in quantum gases. *Nature*, 480:500–503, 2011.
- [45] Bloch I., Dalibard J., Zwirger W. Light-cone-like spreading of correlations in a quantum many-body system. *Nature*, 481:484–487, 2012.
- [46] Zimmermann B., Müller T., Meineke J., Esslinger T., Moritz H. High-resolution imaging of ultracold fermions in microscopically tailored optical potentials. *New Journal of Physics*, 13(043007), 2011.
- [47] Becker C. *Multi component Bose-Einstein condensates: From mean field physics to strong correlations*. PhD thesis, University of Hamburg, 2008.
- [48] Serwane F. The setup of a magneto optical trap for the preparation of a mesoscopic degenerate fermi gas. Master's thesis, University of Heidelberg, 2007.
- [49] Kawanaka J. et al. Quadratic collisional loss rate of a ^7Li trap. *Physical Review A*, 48(2):883–885, 1993.
- [50] Ridinger A. et al. Large atom number dual-species magneto-optical trap for fermionic ^6Li and ^{40}K atoms. *EPJ D*, 65(1-2):223–242, 2011.

- [51] Landini M. et al. Sub-doppler laser cooling of potassium atoms. *Physical Review A*, 84(4):043432, 2011.
- [52] Townsend C.J. et al. Phase-space density in a magneto-optical trap. *Physical Review A*, 52(2):3476–3479, 1995.